Geophys. J. Int. (2007) **170,** 615–634 doi: 10.1111/j.1365-246X.2007.03451.x

Emplacement, growth, and gravitational deformation of serpentinite seamounts on the Mariana forearc

A. J. Oakley,[1] B. Taylor,[1] P. Fryer,[2] G. F. Moore,[1] A. M. Goodliffe[3] and J. K. Morgan[4]

[1]*Department of Geology and Geophysics, SOEST, University of Hawaii, Hawaii, USA. E-mail: aoakley@hawaii.edu*
[2]*Hawaii Institute of Geophysics and Planetology, University of Hawaii, Hawaii, USA*
[3]*Department of Geological Sciences, University of Alabama, AL, USA*
[4]*Department of Earth Science, Rice University, TX, USA*

Accepted 2007 March 23. Received 2007 March 21; in original form 2006 August 17

SUMMARY

Serpentinite seamounts, representing some of the first material outputs of the recycling process that takes place in subduction zones, are found on the outer Mariana forearc. Multichannel seismic (MCS) and bathymetric data collected in 2002 image the large-scale structures of five seamounts, as well as the pre-seamount basement geometry and sediment stratigraphy. We present data from three edifices that provide insights into seamount growth and internal deformation processes and allow us to support the interpretation that serpentinite mud volcanoes are formed by the episodic eruption of mud flows from a central region. The presence of thrust faulting at the base of Turquoise and Big Blue Seamounts, along with the low surface slopes (5°–18°) of all the seamounts studied, lead us to infer that these edifices spread laterally and are subject to gravitational deformation as they grow. Numerical simulations using the discrete element method (DEM) were used to model their growth and the origins of features that we see in MCS sections, such as basal thrusts, inward-dipping reflections and mid-flank benches. The DEM simulations successfully reproduced many of the observed features. Simulations employing very low basal and internal friction coefficients (∼0.1 and ∼0.4, respectively) provide the best match to the overall morphology and structures of the serpentinite seamounts. However the simulations do not capture all of the processes involved in seamount growth, such as withdrawal of material from a central conduit leading to summit deflation; compaction, dewatering and degassing of mud flows; mass wasting in the form of sector collapse and growth upon a dipping substrate. A strong reflection beneath the summit of Big Blue, the largest serpentinite seamount on the Mariana forearc, represents the floor of a summit depression that has been partially in-filled by younger muds, supporting the idea that serpentinite seamounts grow by episodic mud volcanism. Boundaries of mud-flow units are visible in bathymetric data and as normal polarity, subhorizontal reflections on seismic profiles. Big Blue Seamount displays complex nesting relationships as it merges with other seamounts to form a large, composite edifice. Flank flows of serpentinite muds on Big Blue and Celestial Seamounts downlap pre-existing forearc substrate. The interface between serpentinite seamounts and the underlying forearc sediments is represented by a reverse polarity reflection beneath Big Blue and Celestial Seamounts, suggesting that the substrate is undercompacted/overpressured and may be a zone of fluid migration. DEM simulations suggest that this boundary represents a distinct décollement along which the seamounts slide laterally. In contrast, Turquoise Seamount grows laterally, not by stable sliding along the top of forearc sediments, but by incorporating them into large basal thrusts.

Key words: forearc, Mariana, reflection seismology, serpentinite, subduction zone.

1 INTRODUCTION

Oceanic lithosphere is recycled at subduction zones where, with increasing pressure and temperature, compaction, prograde metamorphism and partial melting release fluids into the overriding plate (Morris *et al.* 1990; Bebout & Scholl 1996; Tatsumi 2005). Hydrous fluids liberated beneath the forearc partially serpentinize the overlying mantle peridotite (Peacock 1990; Mottl 1992; Schmidt & Poli 1998; Hyndman & Peacock 2003; Rupke *et al.* 2004). Protrusions of hydrated mantle form serpentinite seamounts on the outer forearc

© 2007 The Authors
Journal compilation © 2007 RAS

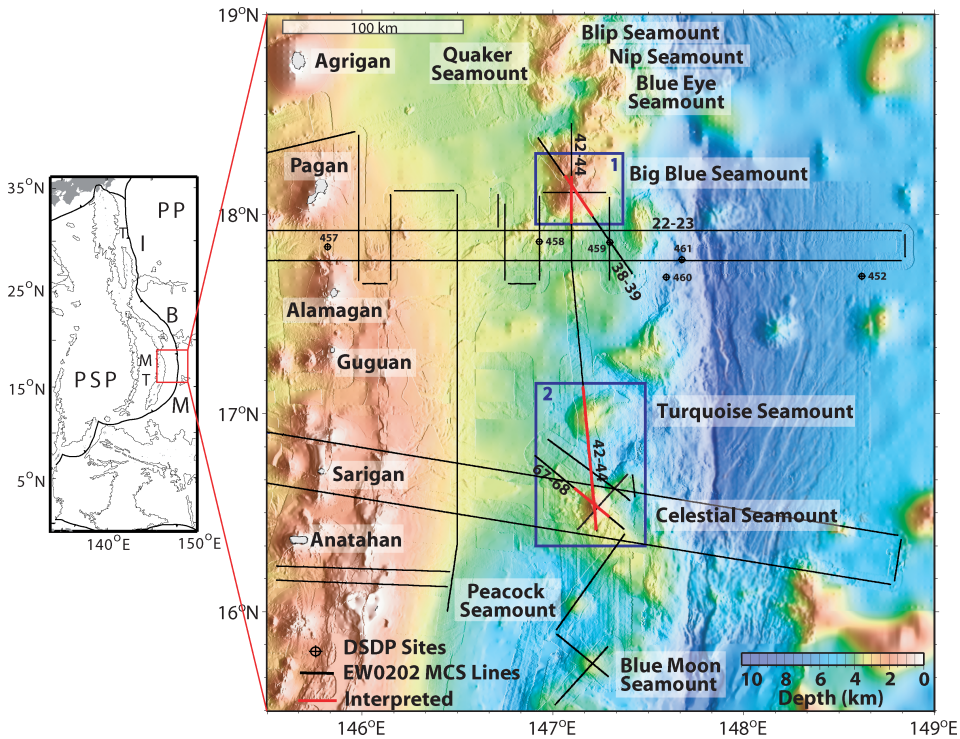

Figure 1. Regional location map. PSP = Philippine Sea Plate, PP = Pacific Plate, IBM = Izu-Bonin-Mariana Trenches, MT = Mariana Trough. Bathymetry of the central Mariana arc-trench system from combined surveys, sunlit from the east, showing EW0202 seismic lines. Interpreted lines are shown in red. Boxes 1 and 2 locate Figs 3, 6 and 7.

of the Izu-Bonin-Mariana (IBM) intra-oceanic subduction system (Fryer & Hussong 1981; Taylor & Smoot 1984; Fryer & Fryer 1987; Horine *et al.* 1990; Fryer & Mottl 1992). Composed of serpentinite muds with entrained ultramafic and mafic clasts, the seamounts expose at the surface forearc mantle and crustal components that originated at depths greater than 20 km (Maekawa *et al.* 1995; Fryer *et al.* 2000; Gharib 2006). Active carbonate and Mg-silicate chimneys and cold-fluid seeps at the summits of many of the serpentinite seamounts provide samples of the chemical precipitates and fluids that result from initial slab devolatilization and supra (above)-slab reactions (Fryer *et al.* 1985; Haggerty 1987; Mottl 1992; Mottl *et al.* 2003; Straub & Layne 2003). Serpentinite seamounts have not yet been found in other active forearcs, but they do have ancient analogues in former convergent margins such as the California Coast Ranges (Hess 1955; Lockwood 1971; 1972; Fryer & Fryer 1987; Macpherson *et al.* 1990; Fryer *et al.* 2000). Understanding how, when and where these seamounts are emplaced is important to correctly characterize the flux of material through the subduction system.

Several researchers have proposed models for the mechanism of emplacement and growth of serpentinite seamounts. Some proposed that serpentinite seamounts are blocks of serpentinized mantle exposed by normal faulting in the forearc (LaGabrielle *et al.* 1992). Others have interpreted the seamounts to be mud volcanoes, that is, low density, buoyant mud and slab-derived fluids extruded onto the seafloor along extensional faults (Fryer 1992b; Fryer & Mottl 1992; Mottl 1992; Phipps & Ballotti 1992). This interpretation is a refinement of the original diapir model that was based on the density contrast between serpentinized material and surrounding crust and mantle (Lockwood 1972; Fryer & Hussong 1981; Bloomer & Hawkins 1983; Fryer *et al.* 1985; Horine *et al.* 1990; Haggerty 1991; Phipps & Ballotti 1992).

Multichannel seismic (MCS) reflection and bathymetric data from serpentinite seamounts on the outer, central Mariana forearc image, for the first time, their structure and their sedimentary and basement substrate. We studied five serpentinite seamounts in this region, including Peacock and Blue Moon seamounts, however, for the purpose of this paper; we will only report a portion of the data for Big Blue, Celestial and Turquoise Seamounts (Fig. 1). The internal structure of serpentinite seamounts in MCS data most often is chaotic, with few coherent reflections. We were able to clearly image basement and sediment reflections beneath the flanks of the seamounts but not directly below their centre. The MCS and complementary bathymetry and side-scan sonar data reveal structures important in seamount growth and deformation and allow us to define key processes in their formation by episodic mud volcanism. We modelled the gravitational deformation of the serpentinite seamounts by constructing 2-D particle dynamics simulations using the discrete element method (DEM). Comparison of these models to the seamount data helped us to recognize internal deformation processes and served as a guide in predicting the interaction between serpentinite muds and pre-existing forearc sediments.

2 GEOLOGICAL SETTING AND PREVIOUS WORK

2.1 IBM subduction and Mariana forearc processes

The IBM region is the classic example of an intraoceanic arc—trench—backarc system (Karig 1971a,b). IBM subduction began about 50 Ma (Taylor 1992; Cosca *et al.* 1998). Currently, the upper-Cretaceous to lower-Jurassic Pacific Plate subducts beneath the Philippine Sea Plate (Fig. 1). The southern IBM arc is isolated from

© 2007 The Authors, *GJI*, **170,** 615–634
Journal compilation © 2007 RAS

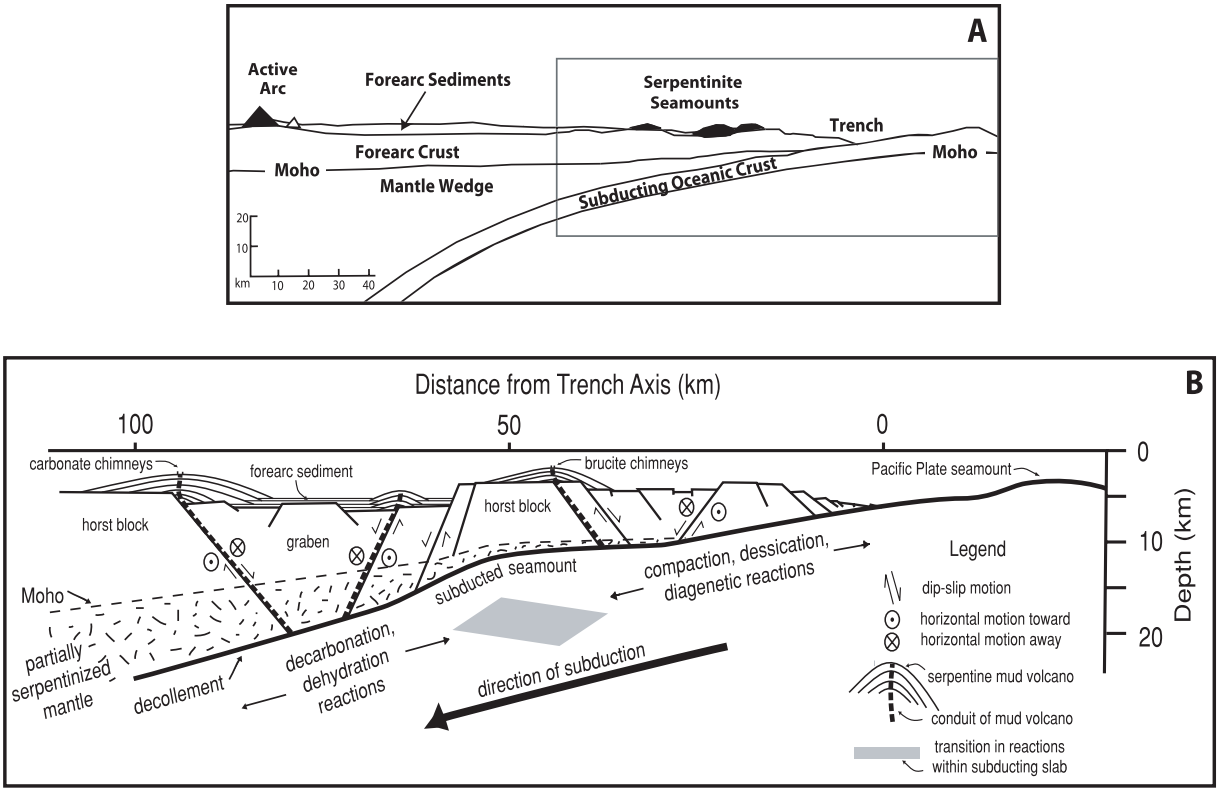

Figure 2. (A) Schematic diagram of the major features of the forearc of an intra-oceanic subduction system. (B) Diagram of the emplacement of serpentinite mud volcanoes on the outer Mariana Forearc. Modified from Fryer *et al.* (2000); no vertical exaggeration.

any continental influence on sedimentation or magmatism and there is no large sedimentary accretionary prism (Hussong & Uyeda 1981; Mrozowski *et al.* 1981; Bloomer 1983).

The central Mariana forearc, from the trench axis to the island arc volcanoes, is 200–220 km wide (Figs 1 and 2). South of 18°N, a line of bathymetric highs ∼40 km to the east of the active volcanoes marks the location of the upper Eocene volcanic chain that, further south, is exposed on the islands from Saipan to Guam (Reagan & Meijer 1984). A thick wedge of volcaniclastic sediments thins eastward and laps onto middle Eocene boninitic and arc tholeiitic basement that was drilled at DSDP Sites 458 and 459 (Mrozowski *et al.* 1981; Cosca *et al.* 1998). Sediment cover on the outer forearc is thin, typically a few tens to hundreds of meters thick, and is often absent on the inner trench slope.

The Mariana forearc is under tension, as indicated by the presence of numerous normal faults that offset both the forearc sediments and the middle-upper Eocene igneous basement (Karig 1971b; Mrozowski & Hayes 1980; Mrozowski *et al.* 1981; Bloomer & Hawkins 1983; Wessel *et al.* 1994; Stern & Smoot 1998). A radial fracture pattern is observed in parts of the forearc, formed as the opening of the Mariana backarc basin increased the radius of curvature of the arc-trench system (Wessel *et al.* 1994; Stern & Smoot 1998; Martinez *et al.* 2000). The origin of an orthogonal set of NE- and NW-trending high-angle faults in the central forearc is less clear.

Numerous serpentinite seamounts are situated on the rugged outer Mariana forearc, 50–120 km from the trench axis (Fig. 1). Fryer *et al*. (1995, 2000) proposed that seamount location is related to the distribution of faults in the supra-subduction zone, the area above the subducting slab, which is in turn governed by the composition and rheology of the forearc wedge. They hypothesized that the brittle outer wedge undergoes vertical tectonism in response to the subduction of Pacific Plate seamounts, creating and/or remobilizing deep-penetrating faults through which hydrated serpentinite muds can reach the seafloor. Alternatively, or in addition, an arcward decrease in the degree of serpentinization of the subforearc mantle may restrict serpentinite seamounts to the outer portion of the forearc (Stern & Smoot 1998; Fryer *et al.* 2000).

The seamounts form as isolated edifices in the south but, for unknown reasons, they are more commonly clustered north of 18°N (Fig. 1). Composite edifices reach heights of 2.4 km and diameters of 40 km; but typical individual seamount dimensions are 1–2 and 15–25 km, respectively. ODP Leg 125 (Sites 778–786) drilled serpentinite seamounts Conical and Torishima as well as sedimented basement on the IBM forearc (Fryer & Pearce 1992). Dredging and coring have shown serpentinite seamounts to be composed of a matrix of serpentinite mud and blocks of serpentinized mafic and ultramafic rocks (Fryer *et al.* 1985; Fryer *et al.* 1990; Horine *et al.* 1990; Fryer 1992b; Fryer & Mottl 1992; Fryer *et al.* 1995). Results from ODP Leg 125 drilling on Conical Seamount, an active edifice located at ∼19.5°N, reveal that the serpentinite formed by hydration of supra-subduction, depleted mantle peridotite (harzburgite) under high-pressure (5–7 kb), low-temperature (<150–250 °C) conditions (Maekawa *et al.* 1992; Maekawa *et al.* 1993; Maekawa *et al.* 1995). Phipps and Ballotti (1992) determined that serpentinite muds drilled from Conical Seamount are extremely weak, plastic solids which, when hydrated, have a density of 1.7–1.8 g cm^{-3}, imparting significant buoyancy relative to the forearc igneous crust.

Material cored from the summit depression on Celestial Seamount is dark-blue, serpentine-rich mud. The high acoustic reflectivity on side-scan images of the edifice, combined with the lack of pelagic sediment cover, suggest that the seamount is currently, or

© 2007 The Authors, *GJI*, **170,** 615–634
Journal compilation © 2007 RAS

was recently active (Fryer *et al.* 2000). In contrast, a core taken near the summit of Turquoise Seamount contained 1.6 m of foraminiferal sand with some volcanic ash and 2 cm of green, oxidized serpentinite mud in the base of the core catcher (Fryer *et al.* 2000). From the core contents, along with the low acoustic reflectivity of the seamount in side-scan sonar data, Fryer *et al*. (2000) concluded that Turquoise Seamount is inactive. Young, active edifices have high-backscatter intensities, whereas older or less active mud volcanoes have a more uniform backscatter character, presumably because of sediment cover. Cores taken at the summit of Big Blue Seamount in 2003 contained fresh serpentinite muds that had not yet been altered by seawater or topped with pelagic sediments, suggesting that the seamount is actively growing (Gharib 2006).

Although nearly vertical below the active Mariana volcanic arc (Katsumata & Sykes 1969; Chiu *et al.* 1991; Engdahl *et al.* 1998; Stern *et al.* 2003), the Pacific Plate descends beneath the outer forearc at shallow angles of ∼7°–10°, calculated from depth sections of our MCS lines that cross the trench (Oakley *et al.* 2005). At shallow depths (<40 km), free water is released from the down-going slab by compaction processes (Peacock 1990; Mottl 1992; Rupke *et al.* 2004). Deeper (down to 200 km) metamorphic dehydration of hydrous slab minerals takes place, producing more fluid (Mottl 1992; Schmidt & Poli 1998; Hyndman & Peacock 2003; Rupke *et al.* 2004). Fluids released beneath the forearc ultimately hydrate the mantle wedge (Fig. 2). The stability of serpentine minerals formed by the hydration of mantle peridotite has been correlated with the regional temperature of the subduction zone. Hydrous minerals are stable over a broad cross-sectional area in cool forearcs (subducting old and cold lithosphere) like that of the IBM system where temperatures in the mantle wedge may be as low as 100–150 °C at 15–20 km depth (Ulmer & Trommsdorff 1995; Hyndman & Peacock 2003).

Hyndman & Peacock (2003), as well as Fryer & Fryer (1987), proposed that early in the history of IBM subduction, sufficient water was released from subducting oceanic crust and sediments to hydrate, and possibly serpentinize the entire forearc mantle. Fryer (1996) and Fryer *et al*. (2000), however, infer that a high degree of serpentinization is inconsistent with the fact that many ultramafic samples recovered from serpentinite seamounts on ODP Leg 125 drilling were only 10 percent serpentinized. These samples provide evidence that even along the conduit of mud volcanoes, the mantle of the overriding plate is not completely serpentinized. Furthermore, preliminary results from an OBS refraction study show sub-Moho velocities 140 km from the trench axis of ∼7.8 km s^{-1}, high enough to argue against pervasive mantle serpentinization beneath the inner forearc (Kerr *et al.* 2002).

Serpentinization is likely to be fracture-controlled, with extensional fault planes serving as conduits for slab-derived fluids in the Mariana forearc (Fryer & Hussong 1981; Bloomer & Hawkins 1983). If so, then the forearc mantle between individual faults may not be greatly affected by serpentinization processes. Although the entire supra-subduction zone mantle may not be uniformly hydrated (Fryer *et al.* 2000), we anticipate that the greatest degree of serpentinization in the forearc region is likely immediately above the slab and near fault surfaces.

2.2 Giant mud volcanoes

In the late 1980s, following Alvin submersible investigations, scientists proposed that IBM forearc serpentinite seamounts are giant mud volcanoes (Fryer & Fryer 1987; Haggerty 1987; Fryer *et al.* 1990), analogous to those formed by the remobilization of sedimentary sequences in accretionary prisms, although different in size, lithology and geochemistry. In the giant mud volcano model (Fryer 1992a; Fryer & Mottl 1992; Fryer *et al.* 1995; Fryer 1996; Fryer *et al.* 1999, 2000), buoyant, hydrated serpentinite muds travel to the surface along forearc faults (Fig. 2). Fryer *et al.* (2000) hypothesized that central conduits may develop at the intersection of fault planes, however, although the seamounts often lie along the trace of major scarps, neither the faults nor the conduits have been directly imaged beneath any of the seamounts in this study. Weak mud flows protrude mainly as a viscous paste flowing over pre-existing forearc crust and sediments, eventually forming a wide, low relief edifice similar in morphology to a shield volcano. Young mud flows, identified in side-scan sonar images, extend as far as 18 km from the summit area of Conical Seamount (Hussong & Fryer 1985; Fryer *et al.* 1990). The geometry of the flank flows seen in the acoustic imagery, as well as variations in backscatter intensities proportional to sediment cover, led Fryer *et al*. (2000) to infer that the seamounts are formed by the episodic upwelling of serpentinite mud. Side-scan sonar images also contain evidence for slope instability on the summit and flanks of the seamounts, such as concentric faults, slumps and debris flows.

The mud volcano model posits that there is a central area of protrusion, although the conduit may migrate over time, possibly along a fault. A rheological study of muds from Conical Seamount suggests that the ultimate strength of the mud is capable of upward transport of serpentinized peridotite blocks as large as 20 m; however, the blocks would sink back into the conduit if the mud ceased upwelling (Phipps & Ballotti 1992). Based on their studies of material drilled from Conical Seamount, Phipps and Ballotti also state that serpentinite muds get stronger and more brittle as they age (1992). Freshly erupted serpentinite mud is unconsolidated and shows yielding and plastic behaviour once deviatoric stresses are applied. More consolidated muds that have been buried and dewatered exhibit some elastic behaviour and have higher yield and ultimate strengths (Phipps & Ballotti 1992). Serpentinite seamounts, like magmatic volcanoes, may be expected to undergo gravitational deformation resulting in summit subsidence, lateral growth and slope failure (Morgan & McGovern 2005a).

3 DATA ACQUISITION AND PROCESSING

In February and March of 2002, we conducted a MCS survey of the central Mariana arc system using the *R/V Maurice Ewing* towing a 6-km, 480-channel streamer cable. Shots were fired every 50 m from a tuned, 6817 in.^{3} array of 20 airguns. The data were recorded in SEG-D format, with a sampling interval of 2 ms. At sea, resampling to 4 ms, application of geometry, trace editing, velocity analysis, inside and outside mutes, stacking and time migration were completed. Additional shore-based processing designed to enhance reflections and remove multiples included methods such as Radon velocity filtering, F-K filtering, and Deconvolution. The data were deconvolved prior to stacking in order to remove false, seafloor parallel reflections created by the airgun bubble pulse. This technique, although successful, had the undesirable effect of partially suppressing the real reflections resulting in a low-amplitude band just below the seafloor. The PROMAX 2-D processing sequence applied to all lines is listed in Table A1.

The seismic lines presented in this paper were time-migrated after muting the seafloor multiple and then converted to depth (except for Line 67–68). Most of the seismic data are displayed in depth with

3× vertical exaggeration. Interval velocities used in these conversions were based upon data from drill sites in the forearc region (Sites 783, Hole A and 779), refraction data, and corrections for velocity 'pull-up.' Details of the depth conversions can be found in Appendix A.

The bathymetric maps used in this study contain Hydrosweep data from the EW0202/03 cruises, Simrad EM300 from a 2003 *R/V Thompson* cruise, 1997 HAWAII MR-1 data, and data from a composite of regional studies conducted on ships from the Japan Center for Marine Earth Science and Technology (JAMSTEC) (N. Seama and M. Nakanishi, private communications, 2002). The bathymetric images are illuminated from the east to highlight relief. Lineations subparallel to ship tracks are data artefacts at the edges of bathymetry swaths resulting from different sound speed profiles used for adjacent data.

4 SERPENTINITE SEAMOUNT DESCRIPTION

Observations from MCS, bathymetric and side-scan sonar data reveal key processes in serpentinite seamount emplacement, growth and gravitational deformation. In this section, we describe the structure, reflectivity and morphology of three seamounts, including details that allow us to infer some material properties and formation processes. In subsequent sections, we will use these descriptions to compare with results from DEM modelling to further develop our interpretation of seamount growth and deformation.

4.1 Big Blue Seamount

Big Blue Seamount, located between 18°N and 18°20′N, centred ∼70 km west of the trench axis, is the largest serpentinite seamount on the Mariana forearc. It is the southernmost edifice in a dense cluster of serpentinite seamounts (Fig. 1). It has an approximate diameter of 40 km, covers an area of roughly 2000 km^2 and reaches a height of 2.4 km above seafloor at its summit. Big Blue is an ovoid composite volcano with an irregular surface expression and slope angles ranging from 6.5° to 13° (Fig. 3). MCS Line 38–39 crosses over the top of Big Blue Seamount which has a more conical portion to the southwest and an irregular-shaped portion with multiple summits and a NE-trending ridge to the northeast (Fig. 3). Although the name Big Blue has traditionally been applied to the entire composite volcano, for the purposes of this paper, Big Blue Seamount will be defined only as the conical portion of the larger edifice, lying primarily to the SW of Line 38–39. The boundaries of Big Blue Seamount and surrounding edifices, Baby Blue Seamount to the north and Grandma Blue Seamount to the east, are interpreted in orange on Fig. 3 and indicated with blue arrows on the following seismic images (Figs 4 and 5).

Bathymetric data show a 2 km wide, 3 km long, oval-shaped, NE-trending depression at the apex of Big Blue Seamount (Fig. 3).

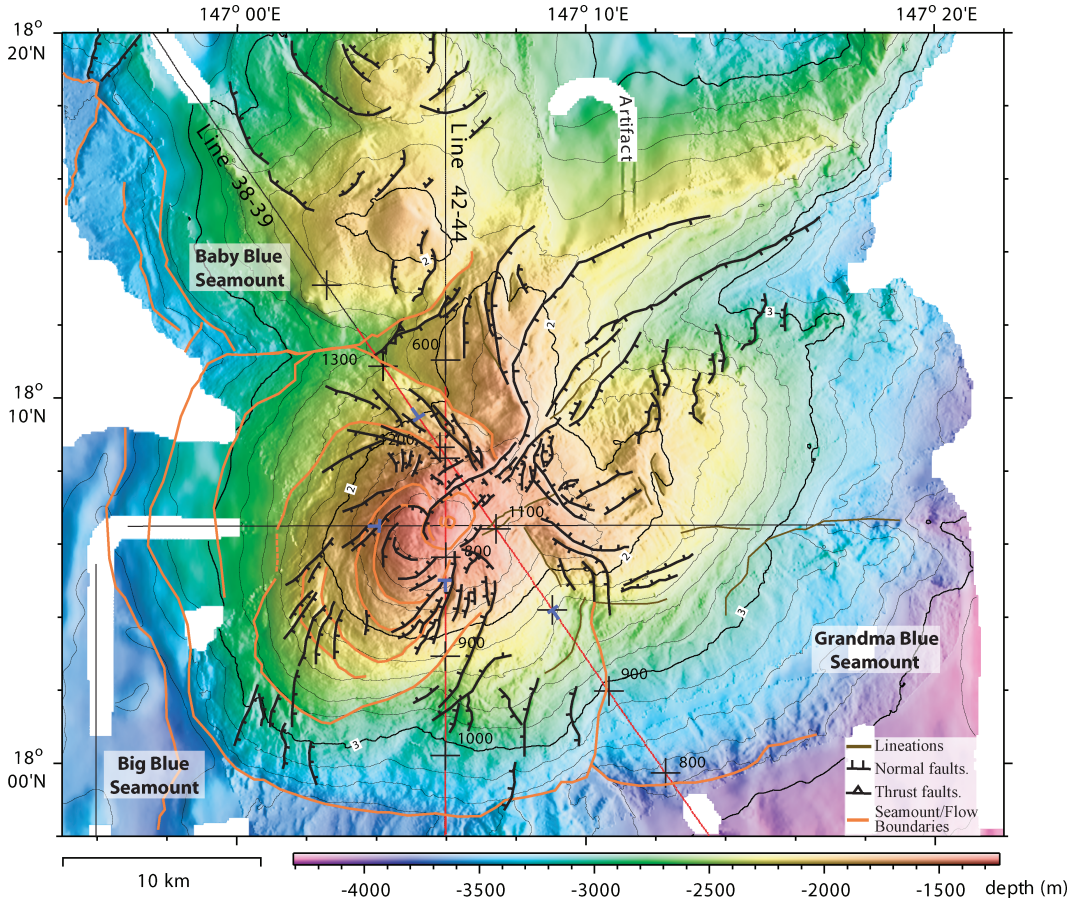

Figure 3. Map of Big Blue Seamount showing locations of seismic lines with shot numbers on interpreted bathymetry (Hydrosweep, MR-1, Simrad EM300 and regional surveys). Interpreted EW0202 lines are shown in red. Contour interval = 200 m. Contour labels in km. A blue T-symbol on the track lines indicates the summit-ward extent to which the interface between forearc sediments and serpentinite can be traced beneath the seamounts.

© 2007 The Authors, *GJI*, **170,** 615–634
Journal compilation © 2007 RAS

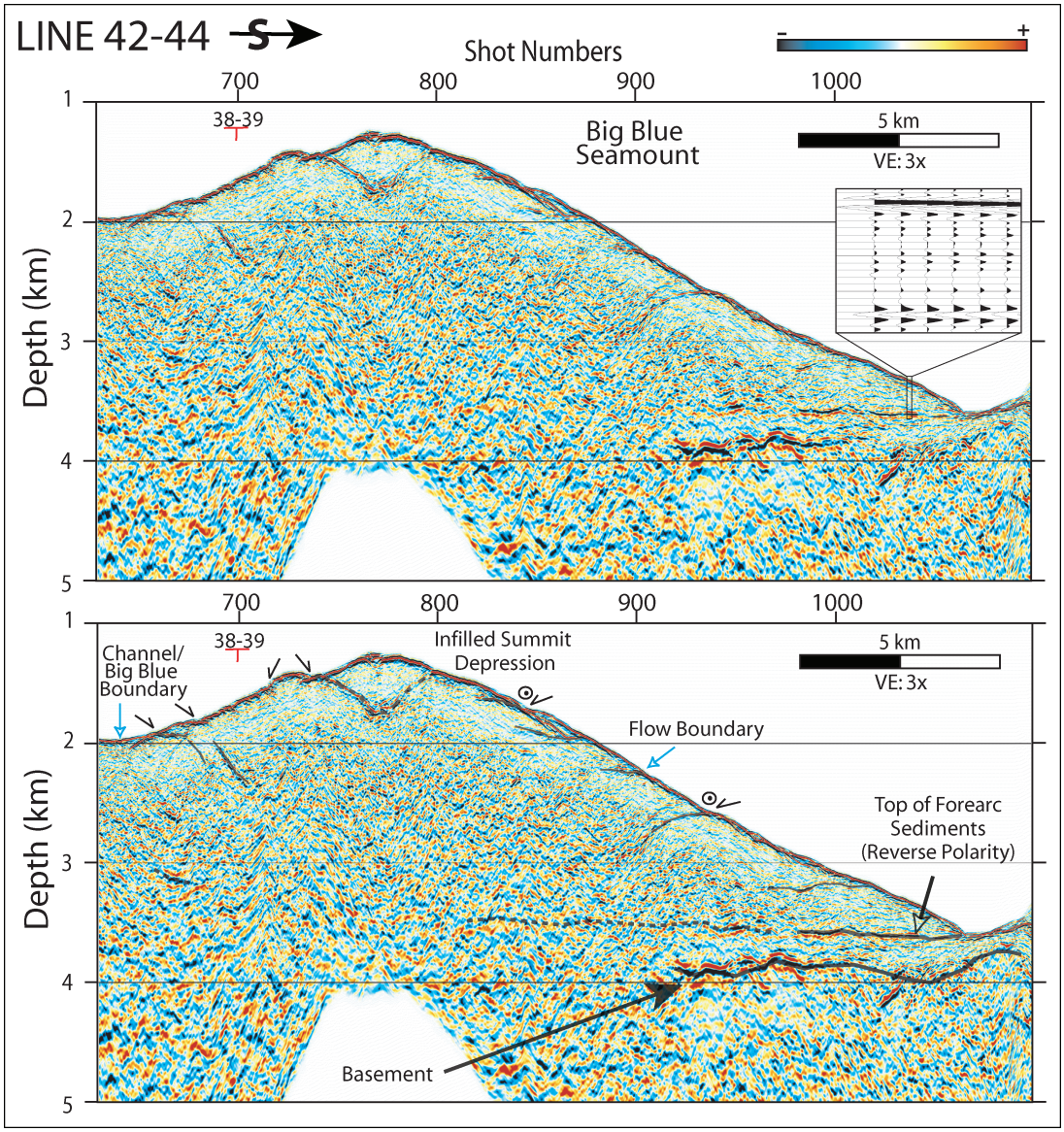

Figure 4. Seismic Line 42–44 (depth converted) over Big Blue Seamount. Normal faulting on the SW flank is related to near surface deformation associated with downhill movement of this sector of the seamount. The reflection at the top of forearc sediments is reverse polarity beneath the southern flank of the seamount. Blue arrows mark flow lobe/seamount boundaries visible in the bathymetry and interpreted on Fig. 3. Black arrows indicate seafloor offset and displacement direction. Location on Fig. 3.

This feature is partially filled in by a dome and is bounded by normal faults. Line 42–44 images the floor of this summit depression as a strong v-shaped reflection beneath seismically transparent material (dashed line on Fig. 4). Detailed bathymetric surveys using a 30 kHz system have identified distinct, lobate flows on the flanks of the mud volcano (interpreted in orange, Fig. 3). These flows are offset by numerous faults. The sense of motion along these faults is determined on the basis of seafloor offset in seismic data and fault scarp geometry in the bathymetry.

Line 42–44 crosses a series of nested, arcuate, convex-downhill fractures that deform the southern slope of Big Blue Seamount (Fig. 3). The high-angle normal faults imaged on the flank bathymetry offset seafloor where they are crossed by MCS lines, but are not visible below the seafloor (Fig. 4). The lack of coherent, subsurface reflections within the serpentinite seamounts makes it impossible to determine the extent of displacement caused by these faults. Where subseafloor reflections are present they are primarily low-angle, discrete segments. The dipping reflection near SP 940 may be related to the normal fault crossed obliquely by Line 42–44. The origins of other dipping reflections imaged in this profile are less clear. Line 42–44 crosses the boundary of a flank mud flow, as indicated by orange lines on Fig. 3 and the blue arrow on Fig. 4 (∼SP 900). The boundaries of mud-flow units are oval-shaped in map view, indicating directional flow. They do not encircle the summit, and are therefore, distinguishable from changes in slope or flank undulations. The flow boundary is represented in the seismic data by a nearly horizontal, normal polarity (same as the seafloor) reflection. At approximately SP 1060, Line 42–44 crosses the distal southern flank of Big Blue Seamount. To the north, the MCS data image a channel that forms the boundary between Big Blue and the more irregular Grandma Blue Seamount to the northeast.

The forearc sediment in this area, overlying a strong basement reflection, is typically less than 0.5 km thick. A reverse polarity (opposite to the seafloor) reflection beneath the southern flanks of Big

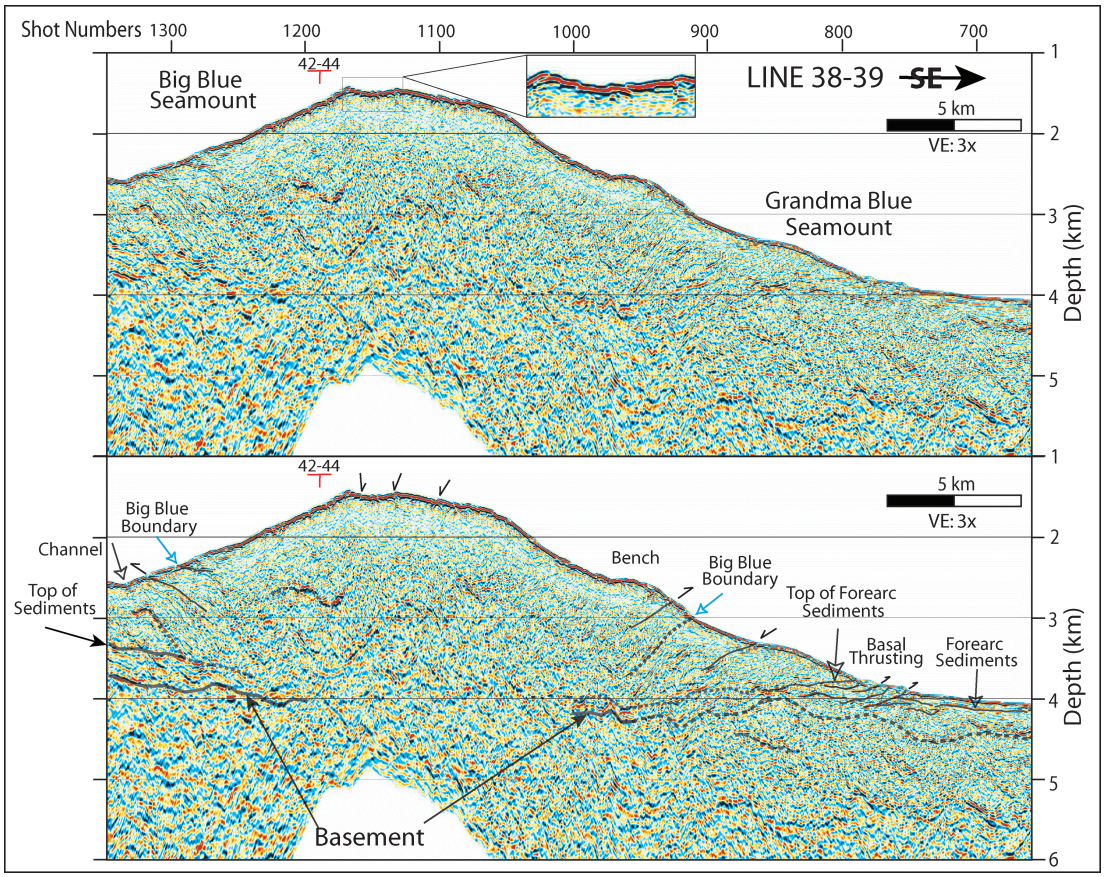

Figure 5. Seismic Line 38–39 (depth converted) over Big Blue Seamount. Basal thrusting is visible on the toe of the SE flank. Blue arrows indicate the boundaries of Big Blue Seamount interpreted on Fig. 3. Black arrows indicate seafloor offset and displacement direction. Location on Fig. 3.

Blue Seamount represents the top of pre-existing forearc sediments (Figs 4 and 5). The reverse polarity of this reflection indicates that forearc sediments under the distal flanks of the seamount have a lower velocity and/or density than the overlying serpentinite mud. Forearc sediment layers beneath the flank are mostly structurally undisturbed by seamount growth. The extent to which the interface between forearc sediments and serpentinite mud can be traced towards the centre of the seamount on seismic sections is indicated with blue T-symbols on Fig. 3. Layered sediments are not imaged beneath the summit or the N/NW flanks where Big Blue merges with other seamounts (Figs 3–5).

Line 38–39 crosses portions of three seamounts that display complex nesting relationships (Figs 3 and 5). Big Blue Seamount overlaps the SW flank of Grandma Blue and both edifices merge with Baby Blue Seamount to the north. To the NW, the seismic line images a channel separating Big Blue Seamount from the northern edifices. Upslope from the channel, the NE-trending boundary between Grandma Blue and Baby Blue Seamounts is interpreted as a thrust fault on Fig. 3. This fault offsets seafloor and creates an inward-dipping reflection at SP 1315 (Fig. 5). On the SE flank, ∼SP 950, a bench, visible in the bathymetry, has formed above a mid-flank reflection that we infer to be a thrust fault based on analogies with DEM simulations (see Section 5). The southeastern boundary of Big Blue Seamount forms an inward dipping reflection at the base of this bench (dashed in Fig. 5). Other dipping reflections are visible further downslope. At the base of Grandma Blue Seamount, beneath a reverse polarity reflection, flat-lying forearc sediment layers are truncated along inward-dipping thrust planes that offset the seafloor.

4.2 Celestial Seamount

Celestial Seamount is located ∼60 km west of the trench at 16°32′N (Figs 1, 6 and 7). Of the three seamounts described herein, Celestial is most similar in morphology to a single magmatic volcano. It is nearly circular with flank slopes ranging from 6.5° to 18°. Celestial Seamount has a diameter of ∼20 km and is topped by a 5 km long, 3.5 km wide, u-shaped summit depression. Celestial sits on the northern edge of a NW-trending basement high and is buttressed to the NE by a ridge/seamount that is thrusting to the NW (Figs 6 and 7). Normal faults drop the summit of Celestial Seamount down to the north, and nested fractures deform the northern flank near SP 4100 on Line 42–44. The western flank of Celestial is steeper and more irregular at its base than the rest of the seamount. The irregular sector of the seamount is bounded to the south by a north-dipping normal fault that extends down the flank of the seamount to its base. Angular blocks outlined in orange (Fig. 6) west of Celestial Seamount are likely debris from the collapse of this flank, whereas more circular features may represent small mud mounds (Figs 6 and 7).

Line 67–68 crosses NW–SE over the summit of Celestial Seamount (Fig. 8). The surrounding forearc sediments, ∼0.6–0.7 s thick, are moderately well stratified and are overlain by small mud mounds to the NW (Fig. 8). At ∼ SP 612, a SE-dipping normal fault offsets sediments and basement beneath a mud mound. Reflections dipping toward the centre of the seamount are imaged on both flanks. The reflection at ∼SP 750 occurs at a break in slope that forms a small bench like that seen on Big Blue Seamount. Above the bench,

© 2007 The Authors, *GJI*, **170,** 615–634
Journal compilation © 2007 RAS

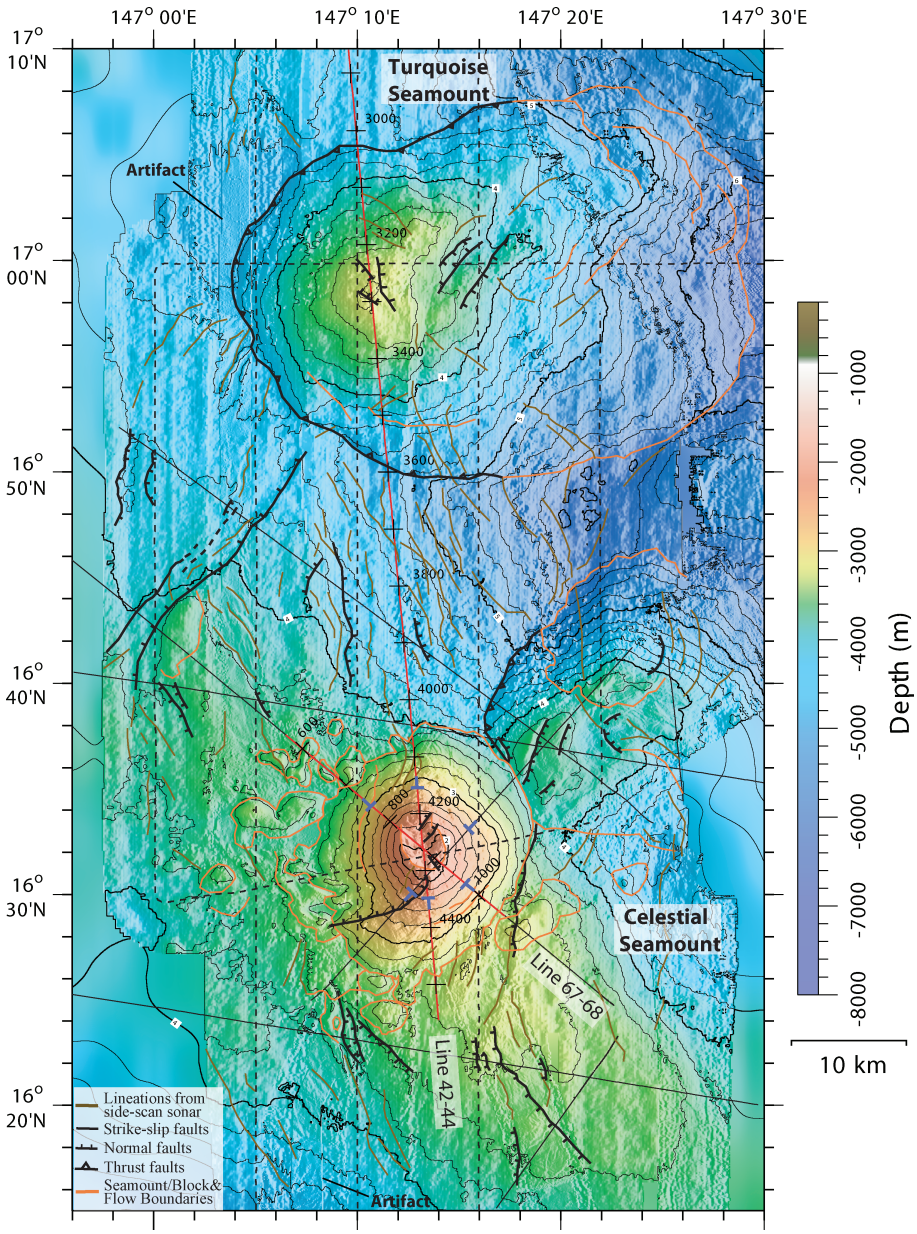

Figure 6. Map of Celestial and Turquoise Seamounts showing locations of seismic lines with shot numbers on interpreted bathymetry (Hydrosweep, MR1, Simrad EM300 and regional surveys). Interpreted seismic lines are shown in red, other MCS tracks from EW0202 are indicated by solid black lines, and six-channel seismic data collected along MR-1 side-scan tracks are represented by dashed black lines. Track subparallel bathymetry lineations are data artefacts. Contour interval = 200 m. Contour labels in km. A blue T-symbol on the track lines indicates the summit-ward extent to which the interface between forearc sediments and serpentinite can be traced beneath the seamounts.

the NW flank of Celestial Seamount is concave up. At ∼Shot Point 980 there is a change in slope of the SE flank of the seamount visible in the bathymetry (Fig. 6). At the base of the section, strong, low frequency mid-crustal reflections are visible ∼1.25 s below basement.

Line 42–44 extends north from Celestial Seamount, across a forearc basin and over the centre of Turquoise Seamount (Figs 9 and 10). This pre-seamount sedimentary basin is a long-lived feature, overlying Eocene basement, with typical sediment thicknesses of 0.7–1.2 km. Basement deepens toward Turquoise Seamount to the north, offset by a series of N-dipping normal faults (Fig. 9). Forearc sediments imaged beneath the southern flank of Celestial Seamount on Line 42–44 onlap southward-shoaling basement, indicating that the seamount protruded through the edge of the sedimentary basin (Figs 9 and 10). Flat-lying, coherent sediment reflections visible under the lower flanks of the seamount are not imaged beneath its upper flanks and summit (Fig. 6). This may be due to difficulties in imaging through thick serpentinite mud; however, it is also likely that beneath the central portion of the seamount, sediment layers are disturbed by seamount growth processes, reducing their coherence and visibility in MCS sections. To the south, near a change in flank slope (∼SP 4350), the sediment horizons gradually become indistinguishable from the chaotic internal structure of the seamount (Fig. 10). Beneath the northern flank of Celestial Seamount, strong, flat-lying sediment horizons terminate abruptly at a series of low frequency, south-dipping reflections between 4 and 5 km depth. The

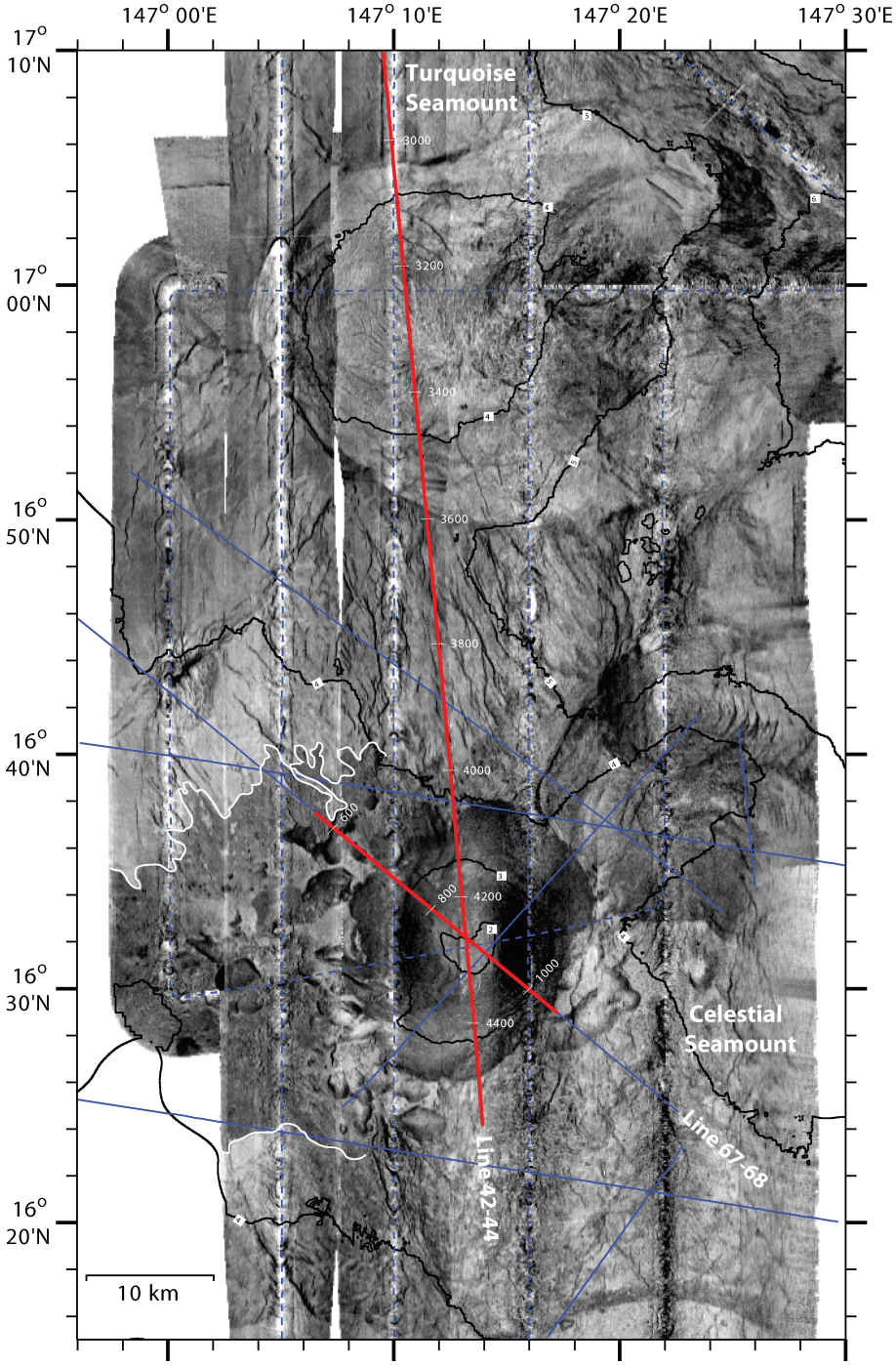

Figure 7. MR-1 side-scan sonar image of Celestial and Turquoise Seamounts with seismic lines. Interpreted seismic lines are shown in red, other MCS tracks from EW0202 are indicated by solid blue lines, and 6-channel seismic data collected during the MR-1 survey are represented by dashed blue lines. Contour interval = 1000 m. Contour labels in km.

southern slopes of Celestial Seamount are concave up and bi-linear with an 8° difference between the upper flank slope (15°) and the lower flank slope (7°) (Fig. 10).

A reverse polarity reflection beneath the flanks of Celestial Seamount represents the top of pre-existing forearc sediments (Figs 8–10). Changes in the slope of this reflection on time sections correlate with changes in seafloor slope and are caused by velocity pull-up under the seamount flanks (Fig. 9). We calculated the minimum velocities for the distal flanks of the seamount that correct for this pull-up and restore the forearc sediments to the regional gradient. These velocities were used for the depth conversion in Fig. 10. The average velocities for the wedge above the reverse polarity reflection range from ~1850 to 2050 m s^{-1} for the lower slope and increase to ~2500 m s^{-1} under the centre of the seamount (as modelled in Fig. A1).

On Line 42–44 (Fig. 9), between Turquoise and Celestial Seamounts, at the base of the section, below 10 s TWTT, there is a prominent, low frequency horizon that we correlate with

© 2007 The Authors, *GJI*, **170,** 615–634
Journal compilation © 2007 RAS

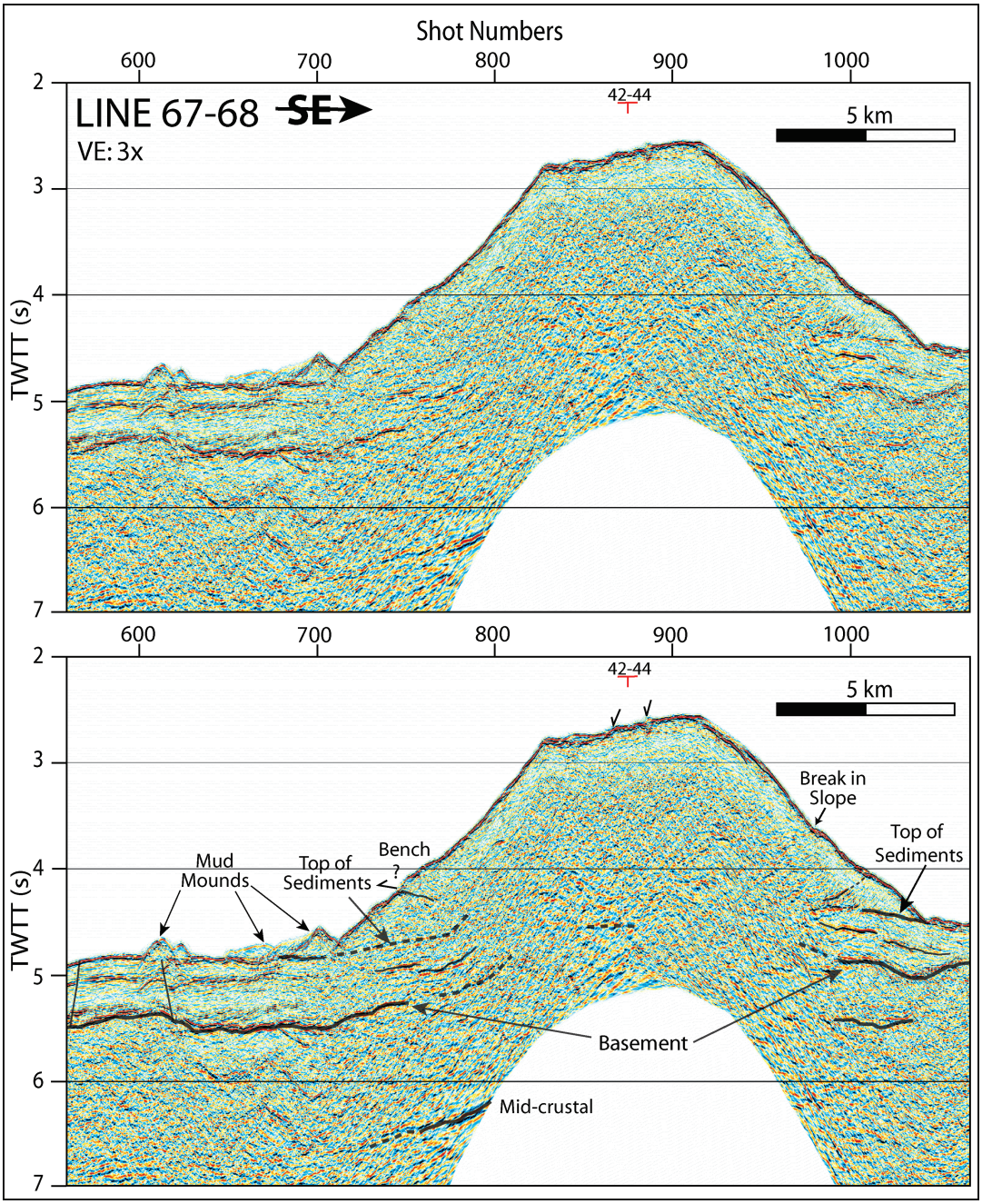

Figure 8. Time section of MCS Line 67–68 across Celestial Seamount. Small mud mounds sit on top of forearc sediments. The NW flank of Celestial is convex upward. The summit of the seamount is deformed by high angle normal faults. Location on Fig. 6.

reflections from the top of the subducting Pacific Plate seen on dip lines (Oakley *et al.* 2005). The downgoing slab is located ~3.5–4 s TWTT below basement between Turquoise and Celestial Seamounts. On crossing lines (not shown) the slab dips an average of 7°–10° and reaches depths of 18–22 km b.s.l. near the serpentinite seamounts (for a range of inferred basement velocities of 5–6.5 km s^{-1}).

4.3 Turquoise Seamount

Turquoise Seamount, at 17°N, is centred approximately 70 km west of the trench axis within a forearc low (Figs 1, 6 and 7). It is an oval-shaped seamount, ~30 km in diameter from N–S, and ~45 km E–W. It has gently (5°–10°) sloping flanks and no obvious summit depression, although the region is offset by normal faults. The eastern portion of the seamount is deformed by parallel, NE-trending normal faults that form a horst and graben. The resulting ridges and valleys fall in line with a 25 km long normal fault and subparallel strike-slip fault (indicated by a flower structure in MCS data) to the southwest of the seamount (Figs 6 and 7). Both faults are currently active as they offset seafloor in seismic, side-scan sonar, and bathymetric data. South of Turquoise Seamount a series of seafloor lineations visible on side-scan sonar images (Fig. 7) primarily trend NW–SE, nearly orthogonal to the large faults discussed above. Where the sense of offset on these lineations is clear on crossing seismic lines, we have indicated the style of faulting (mainly normal faults) on

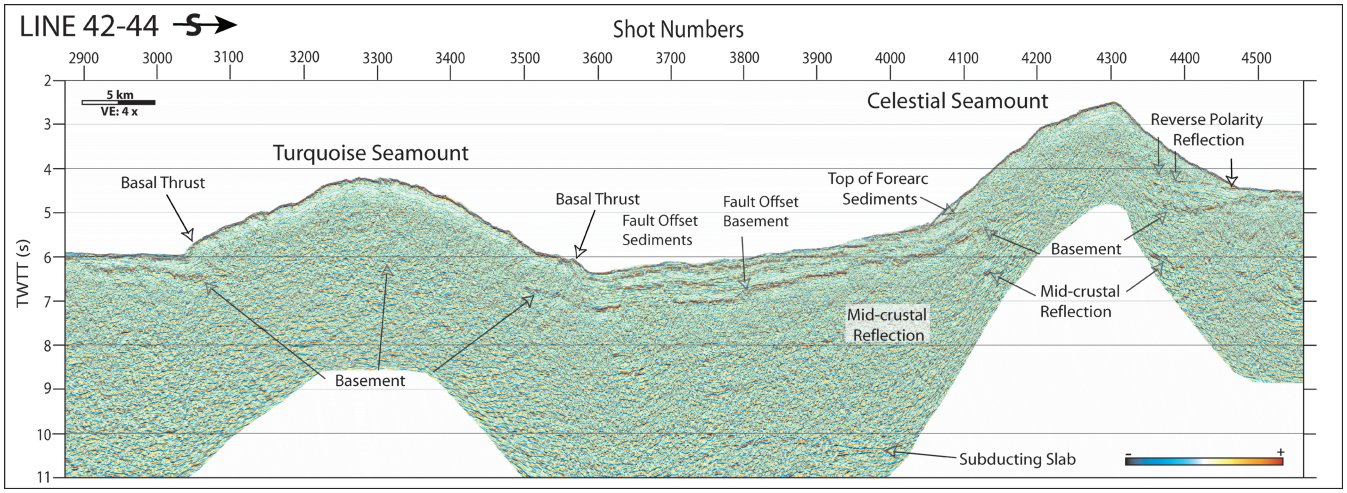

Figure 9. (A) Time migrated MCS Line 42–44 crossing N–S over Turquoise and Celestial Seamounts. Note the change in slope of the reverse polarity reflection beneath Celestial Seamount. TWTT = Two-way travel time. Location on Fig. 6.

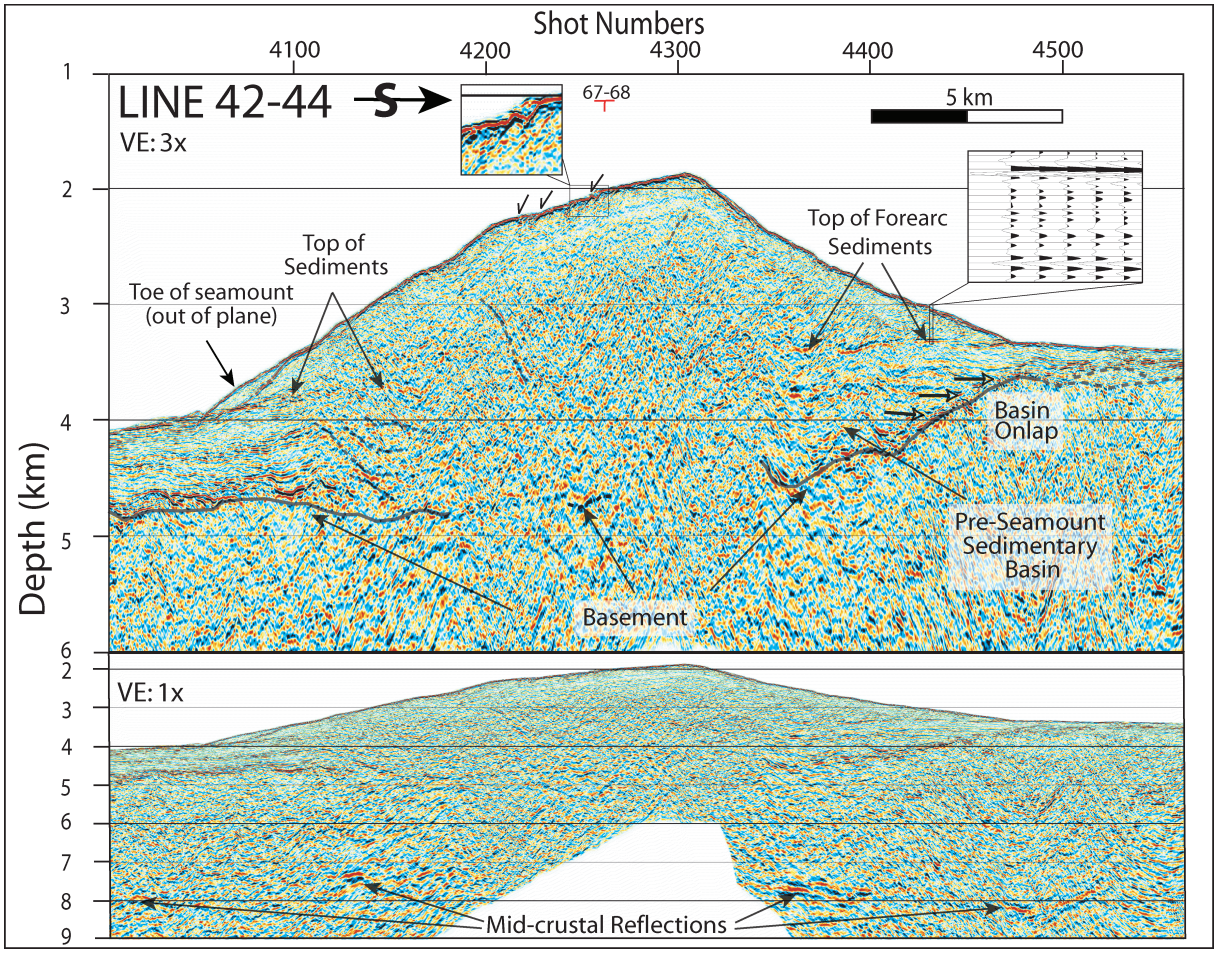

Figure 10. MCS Line 42–44 (depth converted) over Celestial Seamount. Basin onlap is shown on the southern flank. The reverse polarity reflection at the top of forearc sediments is a surface along which the seamount slips. Strong, low frequency, mid-crustal reflections are visible between 7.5 and 8.0 km depth. Line 42–44 intersects with Line 67–68 within the depression at the summit of Celestial. Location on Fig. 6.

Fig. 6. Some of these lineations extend into and offset seafloor on the southern flank of Turquoise Seamount (Figs 6 and 7). Lineations on Turquoise between SP 3100 and 3200 correspond to undulations on the flanks of the seamount visible in MCS data (Fig. 11).

Seismic line 42–44 crosses N–S over Turquoise Seamount (Figs 9, 11 and 12). The basement reflection on Line 42–44 is prominent on the flanks and, although it diminishes in amplitude, is still traceable beneath the centre of the seamount (Fig. 11). The thinning of the

© 2007 The Authors, *GJI*, **170,** 615–634
Journal compilation © 2007 RAS

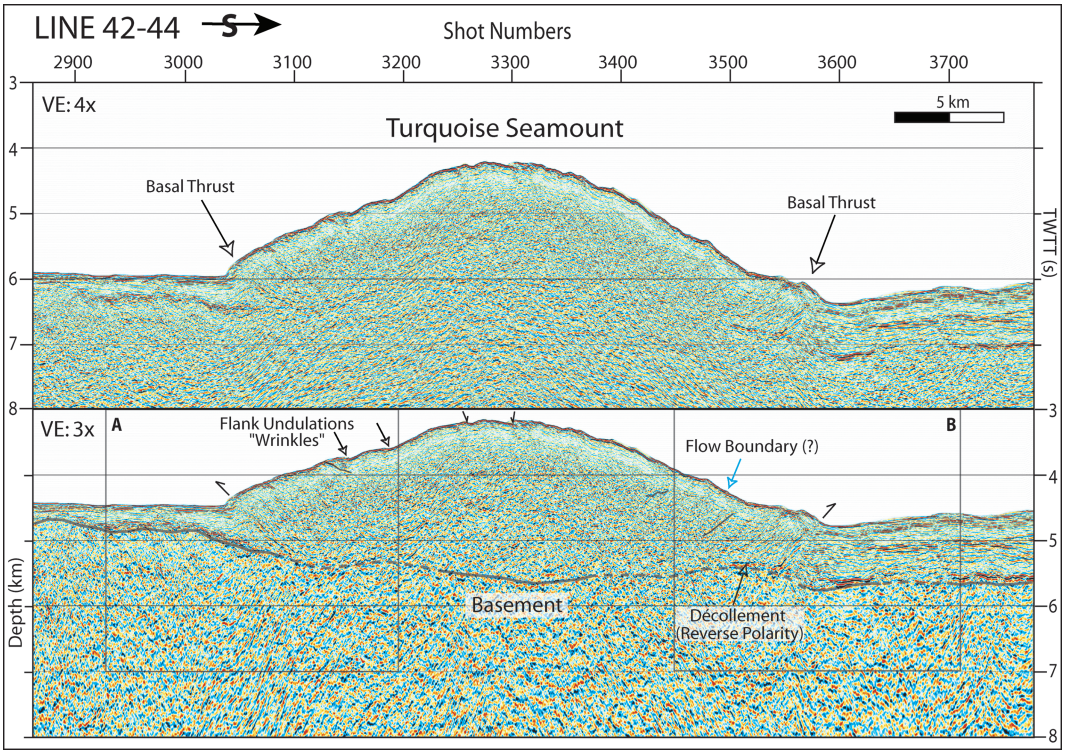

Figure 11. Time and depth sections of MCS Line 42–44 across Turquoise Seamount. A time varying bandpass filter was applied in these images to minimize the negative effects of bubble pulse removal and to enhance shallow reflections. Basal thrusts at the seamount toe displace forearc sediments. Blue arrow indicates a possible mud-flow lobe boundary interpreted on Fig. 6. Boxes A and B refer to areas enlarged in Fig. 12. Location on Fig. 6.

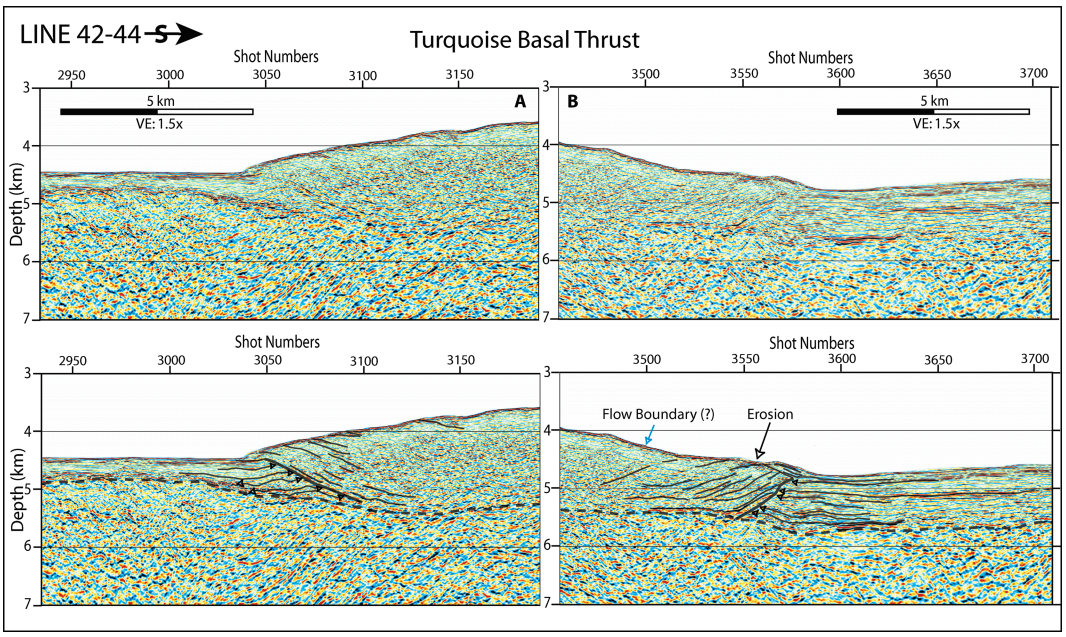

Figure 12. Basal thrusting on the flanks of Turquoise Seamount. Strong, low frequency, dipping reflections separate deformed forearc sediments from truncated flat-lying layers. Sediment layers onlap basement on the northern edge of a large forearc basin.

pre-existing forearc sediment package beneath Turquoise Seamount is a result of onlap onto a shoaling basement (from 5.7 to 4.7 km depth, Fig. 11) that forms the northern edge of a forearc reentrant and basin, discussed above for Celestial Seamount. Just south of SP 3500, Line 42–44 crosses a possible flow lobe boundary visible on side-scan sonar data.

Beneath the distal flanks of Turquoise Seamount, a large thrust fault, terminating at basement, separates inward-tilted reflections in the hanging wall from primarily flat-lying to gently folded sediments in the foot wall (Figs 11 and 12). We interpret the hanging wall reflections to be a thrust package of forearc sediments because mud volcanoes elsewhere, both serpentinite and those found in

accretionary systems, do not display parallel, coherent internal reflections (e.g. Limonov *et al.* 1997; Depreiter *et al.* 2005). The reflection at the base of the deformed sediment package on the southern flank of the seamount appears to be reverse polarity (Figs 11 and 12). No clear décollement is formed beneath the northern flank. The thrust fault approaches but does not offset seafloor on either flank, and erosion has created a seafloor low at the top of the deformed sediments on the southern flank.

The displacement of forearc sediments at the toe of Turquoise Seamount forms a steep basal slope 100–200 m high (Fig. 12). This slope can be traced around the base on the northern, western and southern portions of the seamount (Figs 6 and 7). The flank on the eastern part of Turquoise Seamount has the lowest slope (5°).

5 NUMERICAL SIMULATIONS OF SEAMOUNT GRAVITATIONAL DEFORMATION

5.1 Evidence for gravitational deformation

The presence of thrust faulting at the base of Turquoise and Big Blue/Grandma Blue Seamounts, along with the low surface slopes of all the seamounts studied, lead us to infer that lateral spreading is occurring within the seamounts and that these edifices are subject to gravitational deformation as they grow. We used DEM simulations to model this deformation in the serpentinite seamounts.

2-D DEM simulations of granular piles subject to Coulomb failure provide a first-order look at the deformation modes and deformational geometries that may develop during progressive seamount growth. This method and its application to gravitational spreading are described in detail by Morgan & McGovern (2005a,b), who showed that under uniform basal and internal strength conditions, the granular piles grow self-similarly, developing distinctive stratigraphic relationships, morphologies and structures dependent upon these rheological conditions. Here we expand the application of this method to explore lower strength conditions thought to be representative of serpentinite seamounts, as well as a variety of boundary conditions including seamount growth upon deformable substrates modelled after forearc sediments. We use more numerous particle assemblages in order to yield higher resolution deformation structures.

5.2 Internal and basal strengths of the Seamounts

The previous DEM simulations conducted by Morgan & McGovern (2005a,b) demonstrated that surface slopes of granular piles are strongly dependent on basal friction conditions, and are also good predictors of the mode of gravitational deformation they experience. For example, piles constructed on a strong, cohesive substrate exhibit particle avalanching, outward dipping layers and steep slopes, quite unlike those of the serpentinite seamounts (see fig. 3 in Morgan & McGovern 2005a). Therefore, in order to simulate gravitational deformation of serpentinite seamounts, we needed preliminary estimates of their coefficients of internal and basal friction. Critical Coulomb wedge theory defines a relationship between the sum of surface slope (α) and basal slope (β), that is, the critical taper angle, and the basal and internal friction coefficients (Davis *et al.* 1983). The serpentinite seamounts have consistently low surface slopes of 5°–18°, although the slopes along an individual flank are not constant. Based on the seismic depth conversions, we obtain basal slopes of 0°–2°. Assuming average densities of 1000 and 2200 g cm^{-3} for water and mud, respectively, no overpressure, an internal friction coefficient of 0.30, and our measured α and β values, we iteratively calculated basal friction coefficients using the exact solution by Dahlen (1984). Based on these assumptions, we determined that the low surface slopes on serpentinite seamounts imply very low basal friction coefficients (e.g. $\mu_{\text{bas}} \leq 0.1$). Models employing low coefficients of basal and internal friction reproduce the overall morphology of the serpentinite seamounts.

5.3 Discrete element simulations

The DEM assemblages are composed of homogeneous particles of two different sizes, with radii equivalent to 160 and 120 m, within a domain measuring 50 km across (Figs 13 and 14). Up to ∼12 000 particles are generated in increments of 225, and allowed to settle under gravity to build a granular pile. Particle colours are cycled every four increments to show the stratigraphy. The elastic particles are subject to frictional sliding and, in aggregate, reproduce Coulomb rheology, developing displacement discontinuities that correspond to faults within the pile (Morgan & McGovern 2005a). Basal and internal friction coefficients in these simulations varied from ∼0.10 to 0.30 and ∼0.15 to 0.60, respectively, with low-strength serpentinite muds and their interfaces with forearc sediments falling into the lower ranges of these values (Moore *et al.* 2004). Two basal boundary configurations were used: in the first, granular piles were constructed upon a rigid planar base, assuming no seamount interaction with the substrate (Fig. 13); in the second, piles were constructed upon a pre-existing layer of particles (Fig. 14), to simulate the growth of serpentinite seamounts upon pre-existing forearc sediments.

Two sets of DEM simulations are presented here. Pile growth with an internal friction coefficient of 0.46, constructed upon a rigid, non-cohesive base with a basal friction coefficient of 0.09, develops low surface slopes with concave up morphologies (Fig. 13A). Coloured layers dip outward beneath the summit and are rotated to inward dips beneath the outer flanks. Deep-seated faults extend from the axis of the pile to the basal surface and activate outward sliding of the flanks along a basal décollement (Fig. 13B). Resistance to sliding leads to transient toe thrusts, and local oversteepening of the distal flanks (Stage 12, Fig. 13). Coulomb wedge theory predicts that the seamount will deform until the flank reaches a critical taper at which time it will slide stably. In Stage 13 (not shown), the distal toe of the pile is underlain by a strong décollement and is no longer oversteepened. The cycle is repeated as the shear stress along the base of the pile episodically overcomes basal resistance to sliding, leading to lateral gravitational spreading of the seamount.

The concave up morphologies of the piles are best characterized as bi-linear in form (Fig. 13A). The steeper upper slopes are underlain by active normal faults (Fig. 13B), and have been shown previously (Morgan & McGovern 2005a) to be consistent with critical Coulomb wedges undergoing extension (i.e. limiting slopes of Dahlen 1984). The lower flanks, in contrast, define stable geometries in which the flank cores slide outward with little additional internal deformation (Morgan & McGovern 2005a). The DEM simulations show undulations on the flanks of the seamount that in 3-D would presumably be circumferential. These undulations, or 'wrinkles,' on the surface are related to the internal deformation and lateral spreading of the volcano (i.e. Stage 14, Fig. 13).

Pile growth upon a pre-existing, deformable granular substrate, with internal friction coefficients of 0.3, results in significant substrate thinning beneath the pile, and substrate deformation beneath the distal flanks (Fig. 14A). No single décollement surface is activated in these models. Instead, the high-angle normal faults

© 2007 The Authors, *GJI*, **170,** 615–634
Journal compilation © 2007 RAS

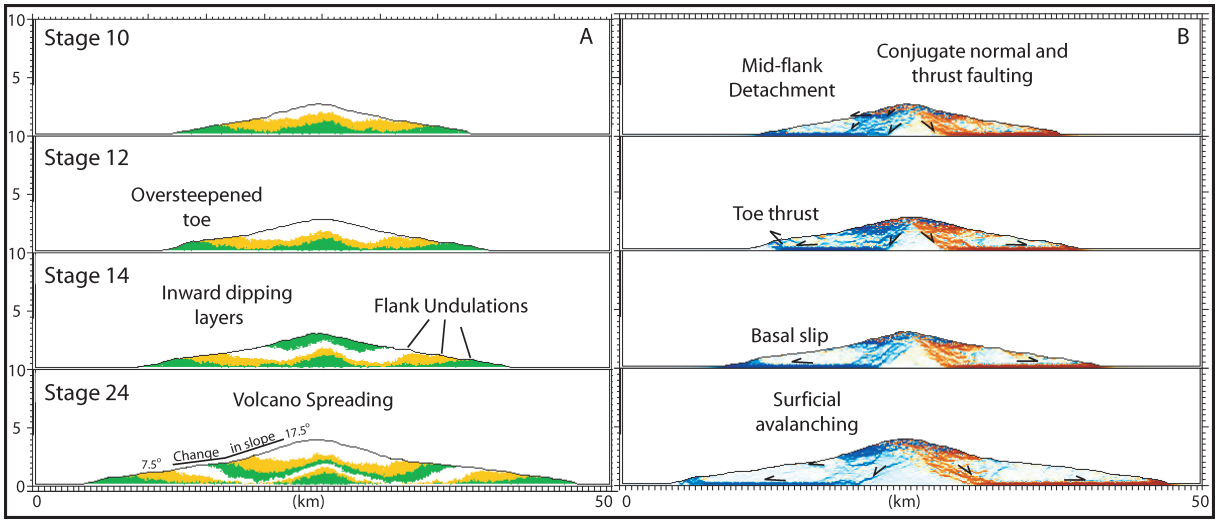

Figure 13. DEM simulation results for an undeformable substrate: μ-base-0.09; μ-internal-0.46. (A) Particle configuration, with alternating colour layers, incrementing from the base of the pile. (B) Incremental displacement discontinuities, showing regions of high shear strain. Red and blue colours denote right- and left-lateral shear strain, respectively, with colour intensity increasing with strain magnitude. Low coefficients of basal friction produce slip along a basal décollement. Low internal friction coefficients result in broad spreading of the edifice which is accommodated by deep-seated normal faulting and summit subsidence. Note the change in slope between the central portion of the seamount where surficial avalanching is occurring and the flanks where basal slip and toe thrusting take place.

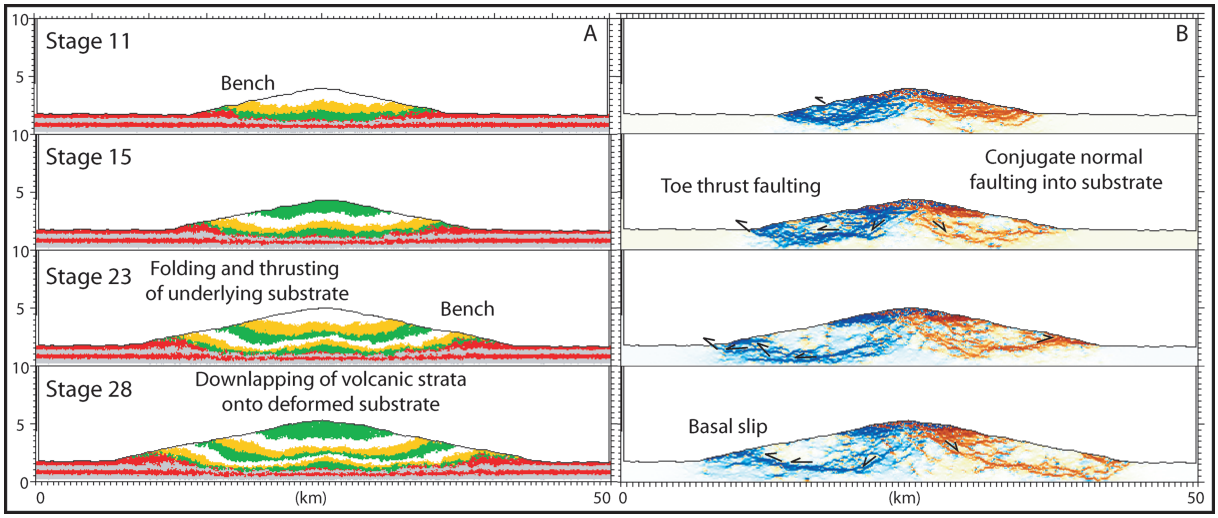

Figure 14. DEM simulation results for a deformable substrate: μ-base- 0.09; μ-internal- 0.30, no cohesion. (A) Particle configuration. (B) Incremental displacement discontinuities, showing regions of high shear strain. Colours as in Fig. 13. Spreading above a deformable substrate allows normal faults to extend into the substrate and incorporate it into the edifice, building small thrust wedges at the toes of the flanks.

beneath the summit extend into the underlying strata, rotating to progressively lower angles with distance from the pile axis, forming thrust faults that emerge near the toe of the pile (Fig. 14B). In this way, thrust slices of the underlying material (red and grey) are accreted to the seamount. The thrust packages at the edge of the simulated seamount are subsequently buried by younger deposits that avalanche down the pile slopes (Fig. 14A).

The surface slope angles in both simulations range from 8° to 17° consistent with those measured for all of the serpentinite seamounts. All modelled simulations are characterized by mid-flank detachments emergent near the change in flank slope.

The DEM simulations presented here are carried out by raining particles from above in 2-D and consequently they do not simulate all of the processes active within growing and deforming serpentinite seamounts. For example, these simulations ignore central conduit intrusion or withdrawal, as well as growth upon a dipping substrate and do not model deformation in the third dimension. Additionally, the modelled particles are homogeneous throughout the granular pile, or within the substrate, and do not reflect temporal and spatial variations in properties that might influence seamount deformation. However, even with these limitations, the simulations provide significant general insight into the characteristics of serpentinite seamount growth and deformation and the interactions of the serpentinite muds and forearc sediments, which are considered in more detail below. Comparison of numerical models to observations enables us to predict the origin of some of the features seen in MCS profiles and to supplement our understanding in areas where data interpretation may otherwise be ambiguous.

6 DISCUSSION

6.1 Growth and deformation of Serpentinite Seamounts

The DEM simulations successfully reproduced the overall morphology of serpentinite mud volcanoes as well as many of the features observed in the data such as basal thrusts, inward-dipping reflections and mid-flank benches. For example, the simulations suggest that bench features like those on the slopes of Big Blue and Celestial Seamounts (Figs 5 and 8) are caused by mid-flank thrusting related to lateral seamount spreading (Fig. 14, Stage 23). In order to provide the best match to the morphology of the serpentinite seamounts, including their low surface slopes of 5°–18°, DEM models require distinctly low basal and internal friction coefficients. Under these conditions, the bi-linear slopes of the modelled piles (Fig. 13) are consistent with the change in slope angle seen on Celestial Seamount (Figs 8–11). In the simulations, such slope changes coincide with the locations of internal detachment faults.

The DEM simulations serve as guides in predicting the interaction between serpentinite material and the forearc substrate, processes that cannot always be directly interpreted from the seismic images. Based on the large thrust packages at the toe of Turquoise Seamount, and the small-scale thrusting on the Big Blue/Grandma Blue edifice, we propose that serpentinite mud volcanoes undergo volcano spreading (e.g. Borgia 1994) and lateral accretion. The DEM simulations demonstrate the feasibility of this process. Instead of sliding along a well-defined décollement at the top of forearc sediments, Turquoise Seamount spreads by displacing pre-existing forearc sediments, forming large thrusts at its base (Figs 11 and 12). Prior compaction and dewatering of these sediments will have increased their strength, (Phipps & Ballotti 1992) allowing them to deform as a coherent package, maintaining the bedding planes we see in the data (Fig. 12). This conclusion is also consistent with the recovery of siltstones (not unlithified sediments or serpentinite muds) in a dredge from the lower western flank of Turquoise Seamount (Bloomer & Hawkins 1983). On Line 38–39 (Fig. 5), thrust slices of forearc sediments are off-scraped and incorporated into the SE flank of the Big Blue/Grandma Blue composite volcano. Again, siltstones were recovered in a dredge from this locality (Bloomer & Hawkins 1983). DEM simulations of pile growth above a deformable substrate show that deformation internal to the pile extends into the substrate, adding thrust slices of the underlying material to the distal toes of the edifice (Fig. 14). In this simulation, there is no cohesion between the base of the model and the substrate (i.e. basement and forearc sediments), therefore, allowing for the incorporation of substrate material into the base of the deforming edifice. The DEM simulation predicts substrate deformation and thinning beneath the edifice by compaction and lateral displacement along thrust faults (Fig. 14, Stages 23 and 28), although these processes are impossible to recognize beneath the chaotic seamount interiors. When cohesion is added, coupling basement and substrate (not shown), the model favours slip along the interface between the substrate sediments and the overlying growing edifice and thinning occurs only by compaction. The DEM simulations, however, do not explain why, when constructed upon the same substrate, one seamount will exhibit thrusting and the other will slide stably as in the case of Turquoise and Celestial Seamounts. The internally stratified sediment package beneath Celestial Seamount is truncated by inward-dipping reflections on the northern flank (Fig. 10). These reflections may be related to faulting internal to the seamount, or may be caused by the displacement of forearc sediment layers, possibly a precursor to a thrust like that at the base of Turquoise Seamount.

Another feature common to both observations and DEM simulations are undulations, or 'wrinkles,' on the flanks of the seamount. In the 2-D simulations, these features are the surface expression of internal deformation caused by seamount settling and lateral growth by thrust faulting (Fig. 13). In 3-D, the undulations are concentric about the flanks of the seamounts. Backscatter images from Conical Seamount provide a good example of concentric ridges on the flanks of a serpentinite mud volcano (see fig. 4 in Fryer *et al.* 1990). Subtle changes in slope are visible on the bathymetric and side-scan data along the flanks of Celestial and Turquoise Seamounts (Figs 6 and 7). Elsewhere, features interpreted on the bathymetry are lobate, ovoid and do not circumvent the seamount, suggesting that they represent individual mud flows, and not 'wrinkles' or slope change in map view (Fig. 3). The majority of such flows have been identified on the SW flank of Big Blue Seamount. Based on bathymetry and side-scan data, we recognized that mud flows forming serpentinite seamounts, unlike the granular packages in DEM simulations, often spread out preferentially in one direction, occasionally extending beyond the bounds of, and therefore covering, the older flows. These flows originate from a central area of protrusion, with the most recent filling in the depression at the summit, providing evidence for the episodic eruption of mud-flow units. The flanks of Big Blue Seamount are deformed by nested normal faults associated with downslope slumping and sliding of young mud flows (Figs 3 and 4).

As an active seamount continues to grow and deform, oversteepening of its flanks compared to its strength can cause mass wasting, both in the form of surficial avalanching (Fig. 13B) and sector collapse. The channelling on the SW flank of Celestial Seamount is likely caused by mass wasting, leading to the deposition of debris piles imaged in the bathymetry and side-scan sonar (Figs 6 and 7). Some of the mud mounds to the west of Celestial Seamount also show evidence of flank collapse. The morphology and low surface slope of the eastern flank of Turquoise Seamount suggest that it may be sliding/slumping downslope toward the Mariana Trench (Fig. 6)

Big Blue Seamount is part of the largest, most complex seamount edifice on the Mariana forearc. To the north and east, the seamount is buttressed by other edifices (Baby Blue and Grandma Blue, respectively), and channels visible in bathymetry and seismic images form boundaries between the seamounts (Figs 3–5). The interaction between coalescing mud volcanoes has caused internal deformation (Figs 4 and 5). Although we have not modelled this type of interaction here, DEM simulations of volcano interactions, applied to Mauna Loa and Kilauea volcanoes on the Island of Hawaii, showed that growth of one volcano upon the flanks of another leads to thinning and spreading of the underlying edifice (Morgan 2006). However, if volcanoes buttress each other, the associated resistance to lateral spreading leads to horizontal compression and formation of low-angle thrust faults at their intersections. Such thrust faulting is visible in the MCS data and bathymetry where the seamounts coalesce (Figs 3–5). Big Blue Seamount is built upon the SW flank of Grandma Blue Seamount, likely causing deformation of that edifice. The normal fault on the lower SE slope of Grandma Blue (∼SP 860) may be related to flank subsidence, and the small-scale thrusting at the base of the seamount indicates lateral spreading (Fig. 5).

6.2 Summit depressions, conduits and faults

The depression at the summit of Big Blue Seamount, bounded by normal faults (Figs 3–5), is likely formed by the dewatering and degassing of serpentinite muds and/or withdrawal of material from the summit of the volcano causing deflation and collapse. The

© 2007 The Authors, *GJI*, **170,** 615–634
Journal compilation © 2007 RAS

depression is partially in-filled by domes of serpentinite mud that were cored in 1997 and 2003 (Fryer *et al.* 1999; Gharib 2006). The strong reflection at the base of the summit depression may be caused by a difference in acoustic impedance related to age and consolidation: fresh, hydrated, gaseous muds are less dense and lower velocity than older, more compacted serpentinites. It is likely that the domes consist of young serpentinite material as the seafloor is devoid of sediment and fresh serpentinite muds cored at the summit were very little altered by seawater (Gharib 2006). This feature provides evidence that serpentinite seamounts grow episodically.

There is active normal faulting in the summit depression at the apex of Celestial Seamount (Figs 6 and 10). The slope of the summit of Celestial Seamount may be caused by mass wasting to the north (Figs 6 and 10). In contrast to Big Blue Seamount, the summit depression has not been filled in by continued mud protrusion. Again, the presence of this depression may be related to the deflation of the summit region caused by degassing of serpentinite muds or the withdrawal of material from a central conduit, indicating either a dormant stage in the formation of Celestial Seamount, or a migration in the path of erupting serpentinite muds depriving the summit region.

Line 67–68 crosses small mud mounds west of Celestial Seamount (Fig. 8). The mounds show variations in degree of backscatter, suggesting differences in degree of sediment cover and, therefore, age (Fryer *et al.* 1999). Some of these mud mounds have been cored, revealing serpentinite material. The normal fault imaged beneath the mound at ∼SP 612 may be a conduit for the upwelling mud indicating that this satellite cone is in the initial stages of mud volcano formation. This is the only place in our data where a fault conduit is directly imaged beneath inferred serpentinite material. Confirmation of the composition and structure of this small mound is necessary in order to determine if it can be considered a serpentinite mud volcano. The strong, irregular boundary between high and low backscatter on the seafloor west of Celestial Seamount is indicated by the white line on the side-scan sonar image, Fig. 7. The shape of the outline and its proximity to both the serpentinite seamount and the small mud mounds suggest that the high backscatter is caused by a recent flow.

The orthogonal fault sets interpreted on the bathymetry in Fig. 6 and visible in the side-scan sonar imagery (Fig. 7) trending toward Turquoise Seamount, lend indirect support to the concept that the conduits of serpentinite mud volcanoes form along intersecting fault planes (Fryer *et al.* 2000). The NE-trending faults to the east of the Turquoise summit may be related to large regional faults of the same trend, although no direct correlation can be made. Lineations extending into the southern flank of Turquoise Seamount offset seafloor and suggest that faulting is actively occurring beneath the edifice (Figs 6 and 7).

6.3 The role of fluids

Water may play an important role in the growth and deformation of serpentinite mud volcanoes and their interaction with the underlying substrate. The interface between the serpentinite seamount and forearc sediments is represented by a reverse polarity reflection at the base of Big Blue/Grandma Blue and Celestial Seamounts. We infer that the sediments are undercompacted (and/or overpressured) beneath the outer flanks of the serpentinite seamounts (Moore *et al.* 1991; Moore & Vrolijk 1992). The sediments in the outer forearc are primarily volcaniclastic turbidities, ash and pelagic muds (Hussong *et al.* 1981). Sedimentation rates are low (6–20 m Myr^{-1}), but vary through time (DSDP Leg 60, Sites 458 and 459). Leg 126 ODP drilling results from the Bonin forearc (Sites 787, 792 and 793) suggest that forearc sediments in the IBM have an average of 50 percent porosity from 500 to 700 m below seafloor (Taylor & Fujioka 1990). Water is released into this system by serpentinite mud and fluids rising along the conduit of the volcano, along with the compaction of forearc sediments beneath the centre of the seamount, where the velocity/density structure increases normally with depth. From either source, fluids will travel along zones of high permeability, following a pressure gradient. In addition to signifying zones where the underlying sediments cannot dewater and are, therefore, overpressured, reverse polarity reflections sometimes indicate pathways of fluid migration, as seen in accretionary prisms (e.g. Moore *et al.* 1991; Moore & Vrolijk 1992). Some of the inward-dipping reflections internal to the serpentinite seamounts, such as those beneath the northern flank of Celestial Seamount (Fig. 10), may represent pathways for fluid to escape from compacting mud.

The DEM simulation above an undeformable substrate (Fig. 13) is consistent with observations made at Celestial and Big Blue Seamounts, suggesting that they are growing laterally by sliding along pronounced décollements at the bases of the seamounts, leaving the underlying material little disturbed. These décollements may be represented by the reverse polarity reflections evident at the top of forearc sediments. On Big Blue Line 42–44 (Fig. 4) the southern flank of the seamount is underlain by a reverse polarity reflection and the distal toe of the flank is oversteepened. This geometry is modelled in DEM simulations that show that intermittent resistance to sliding leads to transient toe thrusts, and local oversteepening of the distal flanks (Stage 12, Fig. 13). The presence of the slip surface at the base of the seamounts may be explained by the presence of high pore pressures in the underlying forearc sediments, caused by the active upwelling of fluids, or introduced with fresh serpentinite muds that reduce the shear strength of the material, decoupling seamount and substrate deformation. Either explanation requires recent or active mud volcanism and fluid migration in the region. Fluid seeps vent slab-derived fluids at the summits of Celestial and Big Blue Seamounts (Mottl *et al.* 2003). These fluids presumably reach the summit along a central conduit through the edifice, and may also flow along the boundary between serpentinite mud and sediments (Fig. 15A). Therefore, we may expect to find chimneys and seeps at the base of the serpentinite seamounts, although, to date these regions have not been explored. Although we only have direct evidence for these two pathways for rising fluid and mud within the seamounts, we cannot rule out the presence of other conduits, sills and intrusions that may contribute to the formation of serpentinite mud volcanoes.

Turquoise Seamount is unique in this region in terms of edifice deformation and interaction with underlying forearc sediments. The fact that Turquoise Seamount, located in a trough, is spreading uphill, whereas Celestial Seamount has formed on a forearc high, may account for their differing interaction with the underlying forearc sediments. This indicates that basal slope, a factor not addressed in the DEM simulations, plays a role in seamount–substrate interactions. Turquoise has the lowest surface slopes of the serpentinite seamounts studied, and the most undulations on its flanks. The overall morphology of Turquoise Seamount, as modelled by DEM simulations, suggests more gravitational spreading compared to Big Blue and Celestial Seamounts. In contrast to the other seamounts, there is no reverse polarity reflection at the top of forearc sediments underlying Turquoise Seamount (Figs 11 and 12). However, the reflection at the base of the deformed sediment package beneath the southern flank appears to be reverse polarity. Backscatter imagery suggests no recent summit eruptions (Fryer *et al.* 2000). Based on seismic and morphologic comparisons with Big Blue and Celestial

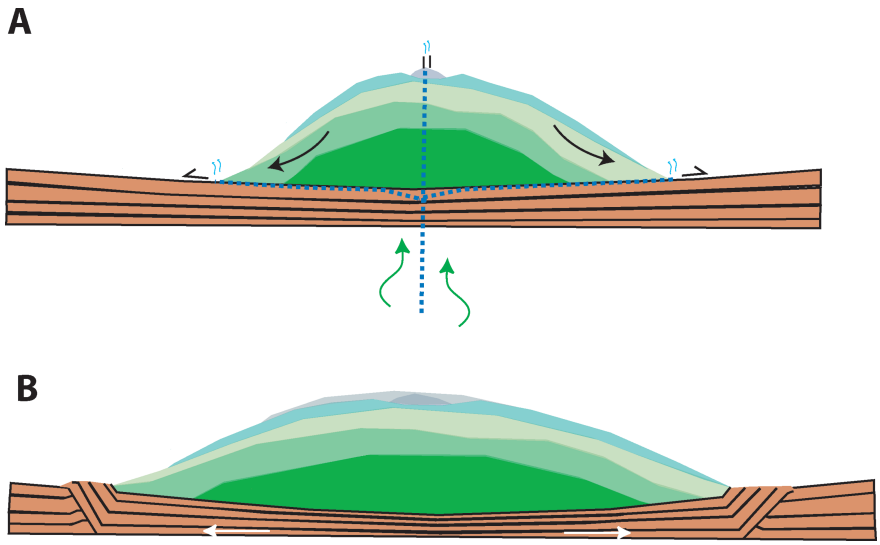

Figure 15. Serpentinite Mud Volcanoes. (A) The seamount is built in a sedimented forearc basin by a series of individual flows fed through a central conduit. A depression at the summit of the seamount is partially infilled by recent mud flows. Carbonate and Mg-silicate chimneys and fluid seeps vent slab-derived fluids at the summit of the seamount. Water produced both by the upwelling of serpentinite mud and fluids, and from the compaction of underlying substrate, may flow along the boundary between serpentinite mud and sediments, reducing shear strength and enabling the seamount to slide laterally. If the underlying sediments are unable to dewater, they will be overpressured and the high pore pressures at the boundary will decouple seamount and substrate deformation. (B) An inactive mud volcano in which all fluid upwelling has ceased. Active fluid seeps and chimneys are not found at the summit and a large basal thrust, the top of which has been eroded, displaces the entire forearc sediment package and accommodates seamount spreading.

Seamounts, and the fact that there are no fluid seeps or fresh serpentinite muds at its summit, we conclude that Turquoise Seamount is not actively growing but is laterally spreading (Fig. 15B). The deformation at the base of Turquoise Seamount is consistent with a fault-bend-fold (e.g. Suppe 1983), the top of which has been partially eroded (Fig. 15B). If Turquoise is inactive, no fresh muds or fluids are flowing through the seamount and substrate; therefore, there are no overpressured sediments or zones of fluid migration along which to slip. In order to grow laterally, Turquoise Seamount displaces the sediments in its path.

6.4 Seamount Composition

The velocities needed to unkink the reflection at the base of the serpentinite seamounts in depth conversions range from an average of 2000 m s^{-1} above the reverse polarity reflection to ~2500 m s^{-1} near the centre of the seamount. Where sampled by drilling and observed in outcrops, serpentinite seamounts are highly heterogeneous, comprised of solid blocks of serpentinite suspended in a mud matrix. Cobbles have been observed in fault scarps (Fryer *et al.* 1985, 1990, 1995; Fryer 1992b; Fryer & Mottl 1992). The core of the volcano may incorporate more blocks/clasts in the mud matrix with an average density higher than that seen at the distal edges. Higher velocities under the centre of the seamount are consistent with a greater proportion of ultramafic blocks there, but may also be related to higher degrees of compaction and deformation of serpentinite material in the core of the volcano.

7 CONCLUSIONS

Our data support the interpretation (Fryer 1992a) that serpentinite seamounts in the Mariana forearc are formed by the episodic eruption of mud flows from a central conduit. The strong reflection beneath the summit of Big Blue Seamount represents a depression that has been partially in-filled by younger muds, supporting the idea that serpentinite seamount growth is episodic. Summit deflation and depression formation may occur when material withdraws from the conduit during inactive periods, and/or by dewatering and degassing of fresh muds. The boundaries of distinct mud-flow units on Big Blue Seamount are visible in both bathymetric and seismic data. Big Blue Seamount displays complex nesting relationships as it overlaps with other seamounts to form a large, composite edifice.

Serpentinite seamounts rest on faulted and sedimented Mariana forearc basement. Although located within the same region of the forearc, and formed above sediments of similar age and composition, the serpentinite mud volcanoes differ in their interaction with the forearc substrate. Big Blue and Celestial Seamounts slide over the top of the pre-existing sediment package, leaving the underlying material largely undisturbed, whereas Turquoise Seamount displaces forearc sediments forming large thrusts at its base. The DEM simulations show that extension of detachment faults into a deformable substrate beneath the growing seamounts provides a mechanism for incorporating thrust slices of the underlying material into the distal toes of the seamount, as interpreted for Turquoise Seamount and the SW flank of Big Blue/Grandma Blue composite seamount. Where this substrate is less deformable, and/or greater fluid pressures enable a pronounced décollement to form, stable sliding occurs. Such is the case beneath the outer flanks of Celestial and Big Blue Seamounts where the reflection at the top of the forearc sediments is reverse polarity. Stable sliding may be explained by the presence of high pore pressures that reduce shear strength along the interface between serpentinite muds and forearc sediments, lowering basal friction and decoupling seamount and substrate deformation. Serpentinite mud and fluids travel to the summit along the conduit of the volcano and may also flow along the interface between serpentinite muds and forearc sediments.

Turquoise is the only seamount imaged in this region of the Mariana forearc that grows laterally, not by sliding stably on top

© 2007 The Authors, *GJI*, **170,** 615–634
Journal compilation © 2007 RAS

of forearc sediments, but by incorporating them into large thrusts at its base. Turquoise Seamount formed in a trough causing it to 'dig into' the sediments at its base as it impinges on the surrounding slopes during lateral growth. From the low slopes of the seamount and its extensive basal deformation we infer, based on DEM simulations, that Turquoise Seamount has undergone more gravitational spreading than Big Blue and Celestial Seamounts. There are no fresh serpentinite muds or fluids found at the summit of Turquoise and bathymetric, seismic and side-scan data do not show evidence for recent mud flows, therefore, it is likely that Turquoise Seamount is not volcanically active.

The recent flows infilling the depression at the summit of Big Blue Seamount, along with the presence of actively venting fluid seeps, suggest that this seamount is currently active. The small mud mound to the west of Celestial Seamount, underlain by a normal fault, may represent a serpentinite mud volcano in the initial stages of formation.

ACKNOWLEDGMENTS

Careful and thoughtful reviews by Emily Chapp, Patricia Cooper, Nathan Bangs and Robert Stern greatly improved this manuscript. Barrie Taylor provided MCS processing assistance that was essential to this project. We would like to thank the captain and crew of the *R/V Maurice Ewing* as well as the other EW0202 cruise participants. We are very grateful to Masao Nakanishi and Nobukazu Seama for supplying bathymetry data that contributed to our regional map. This research was supported by NSF grant OCE-0001978 as part of the MARGINS Program. This is SOEST Contribution 7098.

REFERENCES

Bebout, G.E. & Scholl, D.V., eds, 1996. *Subduction: Top to Bottom*. American Geophysical Union, Washington, DC.

Bloomer, S.H., 1983. Distribution and origin of Igneous Rocks from the Landward Slopes of the Mariana Trench: implications for its structure and evolution, *J. Geophys. Res.,* **88,** 7411–7428.

Bloomer, S.H. & Hawkins, J.W., 1983. Gabbroic and ultramafic rocks from the Mariana Trench: an Island arc ophiolite, in *The Tectonic and Geologic Evolution of the Southeast Asian Seas and Islands, Part 2,* Vol. 27, pp. 294–317, ed. Hayes, D.E. American Geophysical Union, Washington, DC.

Borgia, A., 1994. Dynamic basis of volcanic spreading, *J. Geophys. Res.,* **99,** 717,791–717,804.

Chiu, J.-M., Isacks, B.L. & Cardwell, R.K., 1991. 3-D configuration of subducted lithosphere in the Western Pacific, *Geophys. J. Int.,* **106,** 99–111.

Cosca, M.A., Arculus, R.J., Pearce, J.A. & Mirchell, J.G., 1998. 40ar/39ar and K-Ar age constraints for the inception and early evolution of the Izu-Bonin-Mariana arc system, *The Island Arc,* **7,** 379–395.

Dahlen, F.A., 1984. Noncohesive critical Coulomb wedges: an exact solution, *J. Geophys. Res.,* **89,** 10 125–110 133.

Davis, D., Suppe, J. & Dahlen, F.A., 1983. Mechanics of fold-and-thrust belts and accretionary wedges, *J. Geophys. Res.,* **88,** 1153–1172.

Depreiter, D.J., Van Rensbergen, P. & Henriet, J.P., 2005. Geophysical evidence of gas hydrates in shallow submarine mud volcanoes on the moroccan margin, *J. Geophys. Res.,* **110**.

Engdahl, E.R., Van Der Hilst, R.D. & Buland, R.P., 1998. Global teleseismic earthquake relocation with improved travel times and procedures for depth determination, *Bull. Seis. Soc. Am.,* **88,** 722–743.

Fryer, P. & Hussong, D.M., 1981. Seafloor spreading in the Mariana trough: results of Leg 60 drill site selection surveys, in *Initial Reports of the Deep Sea Drilling Project*, Vol. **60**, pp. 45–55, eds Hussong, D.M. Uyeda, S. *et al.*, U.S. Government Printing Office, Washington, DC.

Fryer, P., Ambos, E.L. & Hussong, D.M., 1985. Origin and emplacement of Mariana forearc seamounts, *Geology,* **13,** 774–777.

Fryer, P. & Fryer, G.J., 1987. Origins of nonvolcanic seamounts in a forearc environment, in *Seamounts, Islands and Atolls*, Vol. 43, pp. 61–69, eds Keating, B. Fryer, P. & BatizaR., American Geophysical Union Monograph Series, Washington DC.

Fryer, P., Saboda, K.L., Johnson, L.E., Mackay, M.E., Moore, G.F. & Stoffers, P., 1990. Conical Seamount: Seamarc II, *Alvin* submersible, and seismic reflection studies, in *Proceedings of the Ocean Drilling Program, Initial Reports, Leg*, Vol. 125, pp. 69–80, eds Fryer, P. Stokking, J.A. *et al.*, U.S. Government Printing Office, Washington DC.

Fryer, P., 1992a. Mud volcanoes of the Marianas, *Sci. Am.,* 46–52.

Fryer, P., 1992b. A synthesis of Leg 125 drilling of serpentine seamounts on the Mariana and Izu-Bonin forearcs, *Proceedings of the Ocean Drilling Program, Scientific Results,* **125,** 593–614.

Fryer, P. & Mottl, M., 1992. Lithology, mineralogy, and origin of serpentine muds recovered from Conical and Torishima forearc seamounts: results of Leg 125 drilling, *Proceedings of the Ocean Drilling Program, Scientific Results,* **125,** 343–362.

Fryer, P. & Pearce, J., 1992. Introduction to the scientific results of Leg 125, *Proceedings of the Ocean Drilling Program, Scientific Results,* **125,** 3–11.

Fryer, P., Mottl, M., Johnson, L., Haggerty, J.A., Phipps, S. & Maekawa, H., 1995. Serpentine bodies in the forearcs of Western Pacific convergent margins: origin and associated fluids, in *Active Margins and Marginal Basins of the Western Pacific, Geophysical Monograph,* Vol. 88, pp. 259–279, American Geophysical Union.

Fryer, P., 1996. Evolution of the Mariana convergent plate margin system, *Rev. Geophys.,* **34,** 89–125.

Fryer, P., Wheat, C.G. & Mottl, M.J., 1999. Mariana Blueschist Mud Volcanism: implications for conditions within the subduction Zone, *Geol.,* **27,** 103–106.

Fryer, P., Lockwood, J.P., Becker, N., Phipps, S. & Todd, C.S., 2000. Significance of Serpentine Mud Volcanism in convergent margins, *GSA Special Paper,* **349,** 35–51.

Gharib, J., 2006. *Clastic Metabasites and Authigenic Minerals within Serpentinite Protrusions from the Mariana Forearc: Implications for Sub-Forearc Subduction Processes,* University of Hawaii, Honolulu, pp. 239.

Haggerty, J.A., 1987. Petrology and geochemistry of neogene sedimentary rocks from Mariana Forearc seamounts: implications for emplacement of the seamounts, in *Seamounts Islands and Atolls, Geophysical Monograph Series 43,* pp. 175–185, eds Keating, B. Fryer, P. Batiza, R. & Boehlert,G. AGU, Washington, DC.

Haggerty, J.A., 1991. Evidence from fluid seeps atop serpentine seamounts in the Mariana Forearc: clues for emplacement of the seamounts and their relationship to Forearc Tectonics, *Mar. Geol.,* **102,** 293–309.

Hess, H.H., 1955. Serpentinites, orogeny, and epeirogeny, *Geological Society of America Special Paper,* **62,** 391–408.

Horine, R.L., Moore, G.F. & Taylor, B., eds., 1990. Structure of the outer Izu-Bonin Forearc from Seismic-Reflection profiling and gravity modeling, *Proceedings of the Ocean Drilling Program, Initial Results*. U.S. Government Printing Office.

Hussong, D.M. & Uyeda, S., 1981. Tectonic processes and the history of the Mariana Arc: a synthesis of the results of deep sea drilling project Leg 60, in *Initial Reports of the Deep Sea Drilling Project*, Vol. 60, pp. 909–929, eds Hussong, D.M. & Uyeda, S. U. S. Government Printing Office, Washington D.C.

Hussong, D.M., Uyeda, S., *et al.*, 1981. *Initial Reports DSDP, 60*. U. S. Government Printing Office, Washington, D.C.

Hussong, D.M. & Fryer, P., 1985. Fore-Arc Tectonics in the Northern Mariana Arc, in *Formation of Active Ocean Margins,* eds. Nasu, N. *et al.*, pp. 273–290. Terra Scientific Publishing Company, Tokyo.

Hyndman, R.D. & Peacock, S.M., 2003. Serpentinization of the forearc mantle, *Earth Planet. Sci. Lett.,* **212,** 417–432.

Karig, D.E., 1971a. Origin and development of marginal basins in the Western Pacific, *J. Geophys. Res.,* **76,** 2542–2561.

Karig, D.E., 1971b. Structural history of the Mariana Island arc system, *Geol. Soc. Am. Bull.,* **82,** 323–344.

Katsumata, M. & Sykes, L., 1969. Seismicity and tectonics of the Western Pacific: Izu-Mariana-Caroline and Ryukyu-Taiwan regions, *J. Geophys. Res.,* **74,** 5923–5948.

Kerr, B., Klemperer, S.L. & Party, E.S.S., 2002. Wide-angle imaging of the Mariana subduction factory, *Eos Trans. AGU,* **83**(47), Fall Meeting Supp.

LaGabrielle, Y., Karpoff, A.-M. & Cotten, J., 1992. Mineralogical and geochemical analyses of sedimentary serpentinites from Conical Seamount (Hole 778a): implications for the evolution of Serpentine Seamounts, *Proceedings of the Ocean Drilling Program, Scientific Results,* **125,** 325–342.

LaTraille, S.L. & Hussong, D.M., 1980. Crustal structure across the Mariana Island Arc, in *The Tectonic and Geologic Evolution of Southeast Asian Seas and Islands,* ed. Hayes, D.E. pp. 209–221. American Geophysical Union, Washington, D.C.

Limonov, A.F., van Weering, T.C.E., Kenyon, N.H., Ivanov, M.K. & Meisner, L.B., 1997. Seabed morphology and gas venting in the Black Sea mudvolcano area: observations with the Mak-1 deep-tow sidescan sonar and bottom profiler, *Mar. Geol.,* **137,** 121–136.

Lockwood, J.P., 1971. Sedimentary and gravity-slide emplacement of serpentinite, *Geol. Soc. Am. Bull.,* **82,** 919–936.

Lockwood, J.P., 1972. Possible mechanisms for the emplacement of alpine-type serpentinite, in *Studies in Earth and Space Sciences: Geological Society of America Memoir 132 (Hess Volume),* ed. Shagam, R. Hess Volume, pp. 273–287.

Macpherson, G., Phipps, S. & Grossman, J., 1990. Diverse sources for igneous blocks in Franciscan Melanges, California Coast Ranges, *J. Geol.,* **98,** 845–862.

Maekawa, H., Shozui, M., Ishii, T., Saboda, K.L. & Ogawa, Y., 1992. Metamorphic rocks from the serpentinite seamounts in the Mariana and Izu-Ogasawara Forearcs, *Proceedings of the Ocean Drilling Program, Scientific Results,* **125,** 415–430.

Maekawa, H., Shozui, M., Ishii, T., Fryer, P. & Pearce, J., 1993. Blueschist metamorphism in an active subduction zone, *Nature,* **364,** 520–523.

Maekawa, H., Fryer, P. & Ozaki, A., 1995. Incipient blueschist-facies metamorphism in the active subduction zone beneath the Mariana Forearc, *AGU Geophysics. Mongr.,* **88,** 281–289.

Martinez, F., Fryer, P. & Becker, N., 2000. Geophysical Characteristics of the Southern Mariana Trough, 11°50′n–13°40′n, *J. Geophys. Res.,* **105,** 16,591–516,608.

Moore, D.E., Locker, D.A., Tanaka, H. & Iwata, K., 2004. The Coefficient of Friction of Chrysolite Gouge at Seismogenic Depths, in *Serpentine and Serpentinites; Mineralogy, Petrology, Geochemistry, Ecology, Geophysics, and Tectonics*, Vol. 8, pp. 525–538, ed. Ernst, W.G. GSA International Book Series.

Moore, J.C., Brown, K.M., Horath, F., Cochrane, G., MacKay, M. & Moore, G., 1991. Plumbing accretionary prisms: effects of permeability variations, *Phil. Trans. R. Soc. London A,* **335,** 275–288.

Moore, J.C. & Vrolijk, P., 1992. Fluids in accretionary prisms, *Rev. Geophys.,* **30,** 113–135.

Morgan, J.K. & McGovern, P.J., 2005a. Discrete element simulations of gravitational volcanic deformation: 1. deformation structures and geometries, *J. Geophys. Res.,* **110**.

Morgan, J.K. & McGovern, P.J., 2005b. Discrete element simulations of gravitational volcanic deformation: 2. mechanical analysis, *J. Geophys. Res.,* **110**.

Morgan, J.K., 2006. Volcanotectonic interactions between Mauna Loa and Kilauea: insights from 2-D discrete element simulations, *J. Volcanol. Geotherm. Res.,* **151,** 109–131.

Morris, J.D., Leeman, W.P. & Tera, F., 1990. The subducted component in Island-Arc-Lavas – Constraints from Be Isotopes and B-Be systematics, *Nature,* **344,** 31–36.

Mottl, M., 1992. Pore waters from serpentinite seamounts in the Mariana and Izu-Bonin Forearcs, Leg 125: evidence for volatiles from the subducting slab, *Proc. Ocean Drilling Program Sci. Results,* **125,** 373–385.

Mottl, M., Komor, S., Fryer, P. & Moyer, C., 2003. Deep-slab fluids fuel extremophilic Archea on a Mariana Forearc Serpentinite Mud Volcano: ocean drilling program Leg 195, *Geochem., Geophys., Geosyst.,* **4**.

Mrozowski, C.L. & Hayes, D.E., 1980. A seismic reflection study of faulting in the Mariana Fore Arc, in *The Tectonic and Geologic Evolution of Southeast Asian Seas and Islands, Geophysical Monograph Series*, Vol. 23, ed. Hayes, D.E. pp. 223–234. AGU, Washington D.C.

Mrozowski, C.L., Hayes, D.E. & Taylor, B., 1981. Multichannel seismic reflection surveys of Leg 60 sites, Deep Sea Drilling Project, in *Init. Repts. Dsdp, 60,* eds Hussong, D.M. & Uyeda, S. pp. 57–69. U.S. Govt. Printing Office, Washington D.C.

Oakley, A.J., Taylor, B., Chapp, E.L. & Moore, G., 2005. Imaging the subducting Pacific Plate beneath the Mariana Forearc, *Eos Trans. AGU,* Fall meeting Supp.

Peacock, S.M., 1990. Fluid Processes in subduction zones, *Science,* **248,** 329–337.

Phipps, S. & Ballotti, D., 1992. Rheology of Serpentinite Muds in the Mariana-Izu-Bonin Forearc, *Proceedings of the Ocean Drilling Program, Scientific Results,* **125,** 363–372.

Reagan, M.W. & Meijer, A., 1984. Geology and Geochemistry of early Arc-Volcanic Rocks from Guam, *Geol. Soc. Am. Bull.,* **95,** 701–713.

Rupke, L.H., Morgan, J.P., Hort, M. & Connolly, J., 2004. Serpentine and the subduction zone water cycle, *Earth Planet. Sci. Lett.,* **223,** 17–34.

Schmidt, M.W. & Poli, S., 1998. Experimentally based water budgets for dehydrating slabs and consequences for Arc Magma generation, *Earth Planet. Sci. Lett.,* **163,** 361–379.

Stern, R., Fouch, M.J. & Klemperer, S.L., 2003. An overview of the Izu-Bonin-Mariana subduction factory, in *Inside the Subduction Factory, Geophysical Monograph,* Vol. 138, ed. Eiler. J. American Geophysical Union.

Stern, R.J. & Smoot, N.C., 1998. A bathymetric overview of the Mariana Forearc, *The Island Arc.,* **7,** 525–540.

Straub, S.M. & Layne, G.D., 2003. Decoupling of fluids and fluid-mobile elements during shallow subduction: evidence from Halogen-Rich Andesite Melt Inclusions from the Izu Arc Volcanic Front, *G-cubed,* **4,** doi:9010.1029/2002GC000349.

Suppe, J., 1983. Geometry and kinematics of fault-bend folding, *Am. J. Sci.,* **283,** 684–721.

Takahashi, N., 2003. Crustal architecture of the Mariana Arc, *Eos Trans. AGU,* Fall meeting Supp.

Tatsumi, Y., 2005. The subduction factory: how it operates in the evolving earth, *GSA Today,* **15,** 4–10.

Taylor, B. & Smoot, N.C., 1984. Morphology of Bonin Fore-Arc Submarine Canyons, *Geology,* **12,** 724–727.

Taylor, B. & Fujioka, K., 1990. *Proceedings of the Ocean Drilling Program, Initial Reports, 126*. Ocean Drilling Program, College Station, TX.

Taylor, B., 1992. Rifting and the volcanic-tectonic evolution of the Izu-Bonin-Mariana arc, in *Proceedings of the Ocean Drilling Program, Scientific Results, 126,* eds Taylor, B. Fujioa, K. *et al.*, pp. 627–651. Ocean Drilling Program, College Station, TX.

Ulmer, P. & Trommsdorff, V., 1995. Serpentine stability to mantle depths and subduction-related magmatism, *Science,* **268,** 858–861.

Wessel, J.K., Fryer, P., Wessel, P. & Taylor, B., 1994. Extension in the Northern Mariana Inner Forearc, *J. Geophys. Res.,* **99,** 15 181–115 203.

APPENDIX A: MCS PROCESSING AND DEPTH CONVERSIONS

Depth conversions

Forearc sediment and basement reflections are 'pulled-up' in time profiles beneath the serpentinite seamounts. The velocities chosen for depth conversion correct for pull-up by making the minimum velocity correction that restored the forearc sediment reflections beneath the flanks of the seamount to a regional gradient. The velocity model used to convert time to depth for Celestial Seamount is shown in Fig. A1. We used a similar model to produce MCS depth sections for Big Blue Seamount. Beneath a 1500 m s^{-1} velocity for the water column, we used velocities of 1600 m s^{-1} plus a gradient of 1500 m s^{-1} s^{-1} in order to have an average velocity of ∼2000 m s^{-1} in the forearc sediments, a value supported by an OBS refraction survey across the Mariana Forearc (Takahashi 2003). The refraction

line of Takahashi follows an ESE-trending MCS line that crosses the northern flank of Celestial Seamount, with modelled average velocities within the seamount of 3000–3500 m s^{-1}. In order to model these values, we applied a starting velocity of 1600 m s^{-1} plus a gradient of 1500 m s^{-1} s^{-1} to the serpentinite seamounts. In addition to this vertical gradient, we added a horizontal gradient of 0.5 m s^{-1} CDP^{-1} (0.08 km s^{-1} km^{-1}) to increase the velocity in the central portion of the edifice. The horizontal gradient starts at the inflection point of the reflection representing the top of forearc sediments under both flanks of the seamount (labelled in Fig. A1 and seen time sections on Figs 8 and 9) and successfully unkinks the horizon in depth sections. This model results in a velocity inversion between serpentinite material and forearc sediments beneath the seamount. The presence of a reverse polarity reflection (defined as having polarity opposite to the seafloor reflection) at the top of forearc sediments beneath the flanks of the seamounts also suggests that there is an impedance (= velocity × density) inversion at this boundary. We applied a 4.0 km s^{-1} velocity to the basement horizon with a vertical gradient of 2.5 km s^{-1} s^{-1} for 0.8 s. At basement + 0.8 s, a velocity of 6.0 km s^{-1} was applied with a gradient of 0.8 km s^{-1} s^{-1} down to the bottom of the profile. The velocities below basement result in an average crustal velocity in the outer forearc of 6.0–6.5 km s^{-1}, a value supported by various forearc velocity models (LaTraille & Hussong 1980; Takahashi 2003).

Pre-stack depth migrations (PSDM) require precise knowledge of the velocity structure in a region in order to create an accurate representation of the seismic data in depth. With no drill well ties for this data set, it was difficult to constrain a velocity model beyond what is geologically reasonable based on known material properties, velocity pull-up relationships, and extrapolation from dill sites in the forearc region. In an attempt to create the most geologically accurate image we applied PROMAX 2-D Pre-stack Kirchhoff Depth Migration to the south flank of Turquoise Seamount (Line 42–44). Ultimately, we found that for the thrust at the base of the seamount, post-stack time migrations converted into depth did a better job of imaging structures in the data than PSDM. Our lack of success with PSDM is likely related to poor velocity constraints in this region. However, velocity model results from iterations performed during the PSDM process allowed us to improve upon the time-migration velocity model used for all of the other seamounts (1.5 km s^{-1} plus a gradient of 0.5 km s^{-1} s^{-1}). For example, in the Turquoise post-stack time migration model we applied a 4 km s^{-1} velocity to the basement horizon to correct for a bow-tie structure beneath this reflection. We also added a horizontal gradient of 0.2 m s^{-1} CDP^{-1} (0.032 km s^{-1} km^{-1}) to increase the velocities in the thrust packages and the centre of the seamount. For the depth conversion of Turquoise Seamount, we applied a vertical gradient of 1.6 km s^{-1} + 1.2 km s^{-1} s^{-1} within the seamount and sediments, calculated to reach approximately 4 km s^{-1} at the basement horizon beneath the seamount. The velocities and gradients applied below basement are consistent with Fig. A1. The geometry of the flanks of Turquoise Seamount differs from that of Big Blue and Celestial Seamounts in that there is no reverse polarity reflection at the top of forearc sediments that experiences velocity pull-up. Since we did not have this constraint for our depth conversion, we did not include the horizontal gradient in depth employed for the other seamounts in order to unkink this horizon.

Table A1. PROMAX 2-D processing sequence.

Resample to 4 ms
Edit bad traces
Geometry
Sort to common mid-point gathers (CMP)
Bandpass filter (4–6-60–70 Hz)
Form supergathers
Velocity analysis
Correct normal moveout
Top mute
Bottom mute
Pre-stack deconvolution
CMP ensemble stack
Bottom mute for migration
Stolt F-K time migration
F-K filter
Automatic gain control
Post-migration depth conversion
Top mute for display

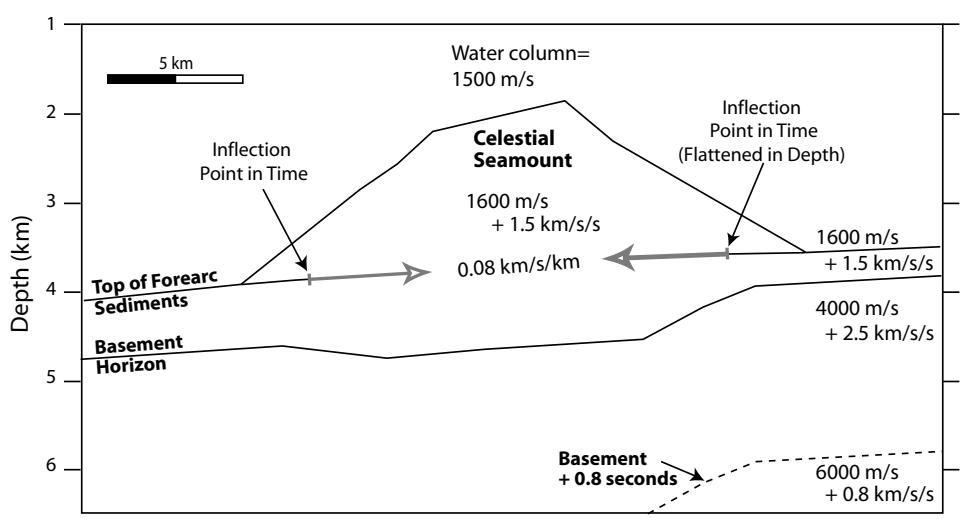

Figure A1. Velocity model for Celestial Seamount depth conversion. In addition to a vertical gradient, we added a horizontal gradient of 0.5 m s^{-1} CDP^{-1} (0.08 km s^{-1} s^{-1}) to increase the velocity in the central portion of the seamount above the pre-existing forearc strata. The horizontal gradient starts in time at the inflection point of the reflection representing the top of forearc sediments under both flanks of the seamount (e.g. Fig. 9). When converted to depth, this reflection is flattened (e.g. Fig. 11). Similar velocity models were used to depth convert Big Blue and Turquoise Seamounts.

© 2007 The Authors, *GJI*, **170,** 615–634
Journal compilation © 2007 RAS